

THE WESTERVELT–RAYLEIGH–PLESSET MODEL OF ULTRASOUND CONTRAST IMAGING WITH MICROBUBBLES: ANALYSIS AND SIMULATION

VANJA NIKOLIĆ[†] AND TERESA RAUSCHER[‡]

ABSTRACT. Ultrasound contrast imaging is a specialized imaging technique that applies microbubble contrast agents to traditional medical sonography, providing real-time visualization of blood flow and vessels. Gas-filled microbubbles are injected into the body, where they undergo compression and rarefaction and interact nonlinearly with the ultrasound waves. Therefore, the propagation of sound through a bubbly liquid is a strongly nonlinear problem that can be modeled by a nonlinear acoustic wave equation for the propagation of the pressure waves coupled via the source terms to a nonlinear ordinary differential equation of Rayleigh–Plesset type for the bubble dynamics. In this work, we first derive a hierarchy of such coupled models based on constitutive laws. We then focus on the coupling of Westervelt’s acoustic equation to Rayleigh–Plesset type equations, where we rigorously show the existence of solutions locally in time under suitable conditions on the initial pressure-microbubble data and final time. Thirdly, we devise and discuss numerical experiments on both single-bubble dynamics and the interaction of microbubbles with ultrasound waves.

1. INTRODUCTION

Ultrasound imaging is a crucial tool in medical diagnostics due to its non-invasive nature, real-time capability, and versatility. However, it has limitations in terms of precision. To address this issue, contrast agents based on microbubbles were introduced. These agents consist of microbubbles with a gas core encapsulated by a shell that resonates and produces echoes when exposed to ultrasound waves. This technique, known as *ultrasound contrast imaging*, shows strong nonlinear effects due to the high-frequency pressure waves in the tissue, the interaction of sound waves with the bubbles, and the behavior of the microbubbles themselves. The bubbles can form, expand, or collapse – a process known as acoustic cavitation. Acoustic cavitation can be non-inertial, involving stable periodic oscillations, or inertial, involving rapid growth and violent collapse of the bubbles. To minimize potential tissue damage, inertial cavitation is typically avoided. Properly managing pressure in the focal region is critical to optimizing the imaging process, that is, ensuring clear images while maintaining safety and effectiveness in ultrasound contrast imaging technologies. In particular, monitoring the nonlinear effects can help maintain the balance between achieving high-quality imaging and minimizing unwanted cavitation effects.

With this motivation in mind, in this work we investigate the complex nonlinear problem of ultrasound contrast imaging from a mathematical side, focusing on non-inertial cavitation. Our main contributions are threefold. They pertain to (i) the derivation of the coupled nonlinear models of ultrasound-microbubble interactions, (ii) their rigorous mathematical analysis, and

2020 *Mathematics Subject Classification.* 35L05, 35L72, 34A34.

Key words and phrases. Westervelt’s equation, Rayleigh–Plesset equation, wave-ODE coupling, ultrasound contrast imaging.

[†]Department of Mathematics, Radboud University, Heyendaalseweg 135, 6525 AJ Nijmegen, The Netherlands (vanja.nikolic@ru.nl).

[‡]Department of Mathematics, Alpen-Adria-Universität Klagenfurt
Universitätsstraße 65–67, A-9020 Klagenfurt, Austria (teresa.rauscher@aau.at).

(iii) their numerical simulation.

The models, derived in Section 2 starting from constitutive laws, are based on a volume coupling of a PDE for the propagation of ultrasound waves with an ODE for the microbubble dynamics. Among them is the system based on the damped Westervelt's equation for the acoustic pressure $p = p(x, t)$ in bubbly media. This wave equation is given by

$$(1.1) \quad ((1 + 2k(x)p)p_t)_t - c^2 \Delta p + \mathcal{A}p = c^2 \eta v_{tt},$$

where $v = \frac{4}{3}\pi R^3$ in the source term denotes the volume of the microbubble with radius R ; see Section 2 for details. Westervelt's equation is capable of capturing prominent nonlinear effects in acoustic wave propagation, such as the steepening of the wave front and generation of higher harmonics. In (1.1), $c > 0$ is the speed of sound in the medium and the coefficient η is related to the number of microbubbles per unit volume. The nonlinearity coefficient $k = k(x)$ is allowed to vary in space, as relevant for imaging applications such as *acoustic nonlinearity tomography* [15, 16]. In (1.1), we incorporate two prominent cases for modeling acoustic attenuation, namely, the strong damping given by

$$(1.2) \quad \mathcal{A}p = -b\Delta p_t$$

with the damping coefficient $b > 0$, and the time-fractional damping given by

$$(1.3) \quad \mathcal{A}p = -b\tau^{\alpha-1} \Delta D_t^\alpha p, \quad \alpha \in (0, 1),$$

where $D_t^\alpha(\cdot)$ is the Caputo–Djrbashian fractional derivative of order α ; see (2.30) below for its definition. In (1.3), $\tau > 0$ is a relaxation parameter. Time-fractional damping (1.3) is known to match better the observed acoustic attenuation in complex media such as soft tissue; see, e.g., [29].

When coupling (1.1) to an equation for the changes in the radius R of the microbubbles, we have various established models to choose from, commonly referred to as Rayleigh–Plesset type equations; see, e.g., [8, 20, 32, 34, 35] and the references provided therein. These equations are derived under the assumptions that the bubble size is much smaller than the pressure wavelength, which, in turn, means we may assume that microbubbles remain spherical as they oscillate. The equations describe the variation of the bubble radius R and can be expressed in the following unified form:

$$(1.4) \quad \rho \left[RR_{tt} + \frac{3}{2} R_t^2 \right] = p_{\text{int}} - p_{\text{ext}},$$

where p_{int} is the internal and p_{ext} external pressure. The latter involves the acoustic input p , dictated by (1.1), and influences the growth and near collapse of the bubble. The coefficient ρ in (1.4) is the mass density of the medium. Depending on the effects they capture, different forms of $p_{\text{int}} = p_{\text{int}}(R, R_t)$ and $p_{\text{ext}} = p_{\text{ext}}(R, R_t, p)$ arise in the literature and lead to different versions of this ODE. We discuss them in detail in Section 2. In the analysis, we consider an equation for the dynamics of microbubbles with a generalized right-hand side that covers these various cases of practical interest; see Section 3. In the simulations, we focus on two concrete versions of Rayleigh–Plesset equations, where we examine both single-bubble dynamics under a sinusoidal driving pressure and the ultrasound-bubble interaction. Details can be found in Section 4.

It is worth mentioning that another potential use of microbubble contrast agents is in targeted drug delivery. This treatment involves introducing microbubbles into the bloodstream and exposing them to high-frequency focused ultrasound waves. As a result, the microbubbles oscillate and collapse, enabling the targeted delivery of drugs that are either attached to the microbubble surface or co-administered in the bloodstream. This method enhances drug concentration at the target site while minimizing systemic side effects, making it a promising approach for treating

various medical conditions such as cancer, cardiovascular diseases, and neurological disorders; see, for example, [28, 31].

Novelty and related mathematical literature. To the best of our knowledge, this is the first mathematical study of models of ultrasound-microbubble interactions. In general, mathematical literature on wave-ODE systems is quite limited. For our theoretical purposes, some helpful ideas can be sourced from other studies of PDE-ODE systems involving the Rayleigh–Plesset equations, in particular [3] and [33].

The mathematical literature on nonlinear acoustic equations for non-bubbly media is, on the other hand, by now quite rich, especially when it comes to the Westervelt equation. In the presence of strong damping (1.2), this equation has a parabolic-like character and its global behavior has been established rigorously in different settings in terms of data; we refer to [12, 24] for the analysis in the presence of homogeneous Dirichlet conditions. Time-fractional dissipation is relatively weak, so only local well-posedness is expected in this case; we point to [15, Theorem 3.1] and [1, Theorem 3.4] for the corresponding results. As the damping coefficient b is relatively small in practice, the limiting behavior of nonlinear acoustic models as this parameter vanishes has also been investigated. A b -uniform well-posedness and the related convergence analysis can be found in [14] and [13] for the strongly damped and fractionally damped Westervelt equation, respectively. Refined versions of nonlinear acoustic models for non-bubbly media, such as the Kuznetsov equation, have also been thoroughly investigated in the mathematical literature; see, for example, [7, 25]. For a detailed overview of mathematical research in nonlinear acoustics, we refer the readers to the review paper [11].

Organization of the paper. The remaining of the present paper is organized as follows. In Section 2, we derive nonlinear acoustic wave equations in bubbly media starting from constitutive laws. We first consider acoustic propagation through thermoviscous liquids and then generalize the derivation to fractional soft tissue media. We furthermore provide an overview of Rayleigh–Plesset models of microbubble dynamics to arrive at coupled wave-ODE systems. Subsequently, we focus our attention on the Westervelt–Rayleigh–Plesset system which we will analyze in Section 3 under homogeneous Dirichlet acoustic boundary conditions by setting up a suitable fixed-point argument. As the settings with strong and time-fractional acoustic attenuation allow for different assumptions on the involved data and coefficient $k = k(x)$, we treat them separately. The main local existence results can be found in Theorems 3.1 and 3.2. Finally, in Section 4 we devise and discuss numerical experiments for both the single-bubble dynamics and the interaction of acoustic pressure waves with microbubbles. Appendix 5 contains auxiliary results on the local Lipschitz continuity of the pressure field as well as the right-hand side in one of the Rayleigh–Plesset equations.

For convenience, we provide an overview of the main physical quantities appearing in this work on the following page. Dimensionless quantities are indicated by writing “[1]” instead of the unit.

PHYSICAL QUANTITIES

α	order of the fractional derivative	[1]
β	nonlinearity coefficient	[1]
\mathbf{u}	liquid and gas velocity	[m/s]
m	gas volume fraction	[1]
χ	shell elasticity	[N/m]
η	coupling constant	[kg/m ⁶]
$\frac{B}{A}$	nonlinearity parameter	[1]
γ	adiabatic index in the tissue	[1]
κ	adiabatic exponent for microbubbles	[1]
κ_s	shell viscosity	[kg/s]
μ	shear viscosity	[Pa s]
μ_b	bulk viscosity	[Pa s]
p_v	vapor pressure	[Pa]
ρ	mass density of the mixture	[kg/m ³]
ρ_g	mass density of the gas	[kg/m ³]
ρ_l	mass density of the liquid	[kg/m ³]
σ	surface tension at the liquid-gas interface of the bubble	[N/m]
σ_0	surface tension of the bubble at rest	[N/m]
τ	relaxation time parameter	[s]
A	amplitude of the driving pressure	[Pa]
b	sound diffusivity	[m ² /s]
c	speed of sound	[m/s]
c_p	heat capacity at constant pressure	[J/K]
c_v	heat capacity at constant volume	[J/K]
f	frequency of the driving pressure	[Hz]
n	bubble number density	[1/m ³]
p	pressure of the liquid	[Pa]
p_{ext}	external pressure	[Pa]
p_{int}	internal pressure	[Pa]
p_{pgn}	gas pressure inside the bubble at rest	[Pa]
p_{stat}	static ambient pressure	[Pa]
R	bubble radius	[m]
R_0	radius at equilibrium	[m]
v	volume	[m ³]

2. DERIVATION OF NONLINEAR ACOUSTIC MODELS IN BUBBLY MEDIA

In this section, we derive a hierarchy of second-order wave equations for the propagation of sound through a bubbly media starting from a governing system of equations and then couple them to models of microbubble dynamics. To this end, we introduce the following quantities, which are decomposed in their mean and alternating part denoted by \cdot_0 and \cdot' , respectively:

$$\begin{aligned}
 \text{density of the mixture:} \quad & \rho = \rho_0 + \rho', \\
 \text{density of the liquid:} \quad & \rho_l = \rho_{l0} + \rho'_l, \\
 \text{pressure of the liquid:} \quad & p = p_0 + p', \\
 \text{gas volume fraction:} \quad & m = m_0 + m', \\
 \text{liquid and gas velocity:} \quad & \mathbf{u} = \mathbf{u}', \\
 \text{bubble number density:} \quad & n = n_0 + n', \\
 \text{bubble radius:} \quad & R = R_0 + R'.
 \end{aligned}$$

In our setting the bubbles are assumed small and densely distributed such that they determine the properties of a continuum mixture of density ρ . The volume concentration of microbubbles is assumed to be uniform. As m is the gas volume fraction, that is the fraction of unit volume of mixture occupied by microbubbles, we have

$$(2.1) \quad m = nv \quad \text{with} \quad v = \frac{4}{3}\pi R^3,$$

where n is the bubble number density, or more precisely the concentration of bubbles per unit volume, and R the bubble radius. Then the continuum density is given by

$$(2.2) \quad \rho = (1 - m)\rho_l + m\rho_g,$$

where ρ_l and ρ_g are the liquid and gas densities in a suspension of gas bubbles in liquid, respectively. We assume that the mean pressure p_0 is the same in bubbles and liquid and that all bubbles have the same equilibrium radius R_0 .

2.1. Approach in the derivation. In the upcoming derivations, we adopt the approach of Crighton described in [6], following Lighthill's scheme introduced in [23] and elaborated by Blackstock in [4]; see also [10, Ch. 5]. According to this approach, we distinguish three categories of contributions:

- First order. First-order contributions are terms that are linear with respect to the fluctuating quantities $(\cdot)'$ and do not relate to dissipative effects.
- Second order. Second-order contributions are linear dissipative terms and terms that are quadratic with respect to fluctuating quantities.
- Higher order. All remaining terms are considered to be of higher order.

The fundamental rule in Lighthill's approximation scheme is that one should keep first- and second-order terms while higher order contributions are neglected. A further approximation rule that we make use of below is the *substitution corollary* that permits us to substitute each term with second- or higher-order terms with its first-order approximation.

In addition, we assume in this section that the fluctuating quantities are zero at initial time.

2.2. Derivation of acoustic equations in bubbly liquids. The acoustic field is fully described by the conservation of mass for the mixture

$$(2.3) \quad \rho_t + \nabla \cdot (\rho \mathbf{u}) = 0,$$

the conservation of momentum for the mixture

$$(2.4) \quad \rho(\mathbf{u}_t + (\mathbf{u} \cdot \nabla) \mathbf{u}) + \nabla p = \mu \Delta \mathbf{u} + \left(\frac{\mu}{3} + \mu_b \right) \nabla(\nabla \cdot \mathbf{u}),$$

where μ is the shear viscosity and μ_b the bulk viscosity in the medium, the conservation of bubbles

$$(2.5) \quad n_t + \nabla \cdot (n\mathbf{u}) = 0,$$

and the state equation

$$(2.6) \quad \rho'_l = \frac{p'}{c^2} - \frac{1}{\rho_{l0}c^4} \frac{B}{2A} p'^2 - \frac{\gamma}{\rho_{l0}c^4} \left(\frac{1}{c_v} - \frac{1}{c_p} \right) p'_t,$$

where c is the speed of sound, $\frac{B}{A}$ denotes the parameter of nonlinearity and γ the adiabatic exponent. Further, c_v and c_p are the specific heat capacity at constant volume and constant pressure, respectively.

The gas contribution $m\rho_g$ to ρ is relatively small and can therefore be neglected (following, e.g., [6, Sec. 4]), such that (2.2) reduces to

$$(2.7) \quad \rho = (1 - m)\rho_l,$$

and thus we have

$$\rho_0 = (1 - m_0)\rho_{l0}, \quad \rho' = (1 - m_0)\rho'_l - \frac{m'\rho_0}{1 - m_0}.$$

The gas contribution of the pressure will be incorporated in the ODE for the bubble radius. Recalling that the gas volume fraction is $m = nv$, its mean and alternating parts are given by

$$m_0 = n_0 v_0, \quad m' = n_0 v' + v_0 n' + n' v'.$$

Equations (2.1), (2.3), (2.4), (2.5), (2.6) and (2.7) together with an ODE for the bubble radius are a set of seven equations for the seven fluctuations $(\rho', \rho'_l, p', m', \mathbf{u}, n', R')$. Now, the goal is to approximate this system of equations by one wave equation for the pressure p' and equip it with a Rayleigh–Plesset equation for the radius R of microbubbles to altogether arrive at a coupled system that describes the propagation of sound through a bubbly liquid.

We start by noting that below we only use the linearized approximation of equation (2.5) for the conservation of microbubbles; see (2.12). We proceed by approximating other constitutive equations and then combining them.

2.2.1. Simplifying the conservation of momentum equation. Consider equation (2.4). Recalling the following vector identities on a convex domain:

$$(\mathbf{u} \cdot \nabla) \mathbf{u} = \frac{1}{2} \nabla(\mathbf{u} \cdot \mathbf{u}) - \mathbf{u} \times \nabla \times \mathbf{u}, \quad \nabla(\nabla \cdot \mathbf{u}) = \Delta \mathbf{u} + \nabla \times \nabla \times \mathbf{u},$$

and substituting (2.7) into (2.4), we obtain

$$(1 - m)\rho_l \left(\mathbf{u}_t + \frac{1}{2} \nabla(\mathbf{u} \cdot \mathbf{u}) \right) + \nabla p = \left(\frac{4}{3}\mu + \mu_b \right) \Delta \mathbf{u},$$

where certain terms on the right-hand side are neglected as they decay exponentially away from boundaries and eventually become small compared to the corresponding first- and second-order terms, according to [10]. The decomposition of the quantities into their mean and fluctuating parts, and recalling that $\nabla p_0 = 0$, leads to

$$(2.8) \quad \begin{aligned} (1 - m_0)\rho_{l0}\mathbf{u}_t + \nabla p' &= \rho_{l0}m'\mathbf{u}_t - (1 - m_0)\rho'_l\mathbf{u}_t \\ &\quad - \frac{(1 - m_0)}{2}\rho_{l0}\nabla(\mathbf{u} \cdot \mathbf{u}) + \left(\frac{4}{3}\mu + \mu_b \right) \Delta \mathbf{u}. \end{aligned}$$

Here the first-order terms appear on the left hand-side, second-order terms are collected on the right-hand side and higher-order terms have been neglected.

Next, we make use of the substitution corollary, which means that we are allowed to substitute any physical quantity in a second-order term by its linear approximation since the resulting errors will be of third order. More precisely, we use the following relations:

$$(2.9) \quad \text{linear state equation:} \quad \rho'_l = \frac{p'}{c^2}$$

$$(2.10) \quad \text{linear momentum equation:} \quad \rho_0 \mathbf{u}_t + \nabla p' = 0$$

$$(2.11) \quad \text{linear continuity equation:} \quad \nabla \cdot \mathbf{u} = -\frac{1}{\rho_0} \rho'_t = -\frac{1-m_0}{\rho_0 c^2} p'_t + \frac{1}{1-m_0} m'_t$$

$$(2.12) \quad \text{linear conservation of bubbles:} \quad \nabla \cdot \mathbf{u} = -\frac{1}{n_0} n'_t$$

as well as the identity $p' p'_t = \frac{1}{2} (p'^2)_t$. The terms on the right hand-side of equation (2.8) can therefore be approximated as follows:

$$\begin{aligned} \rho_{l0} m' \mathbf{u}_t &\approx -\frac{\rho_{l0}}{\rho_0} m' \nabla p' = -\frac{1}{1-m_0} m' \nabla p', \\ -(1-m_0) \rho'_l \mathbf{u}_t &\approx -\frac{1-m_0}{c^2} p' \mathbf{u}_t = \frac{1-m_0}{\rho_0 c^2} p' \nabla p' = \frac{1-m_0}{2\rho_0 c^2} \nabla p'^2, \\ \left(\frac{4}{3}\mu + \mu_b\right) \Delta \mathbf{u} &\approx \left(\frac{4}{3}\mu + \mu_b\right) \left(-\frac{1}{n_0} \nabla n'_t\right), \end{aligned}$$

and we can also rely on the fact that $-\frac{1-m_0}{2} \rho_{l0} \nabla (\mathbf{u} \cdot \mathbf{u}) = -\frac{\rho_0}{2} \nabla (\mathbf{u} \cdot \mathbf{u})$. In this manner, from (2.8) we arrive at its approximate version given by

$$(2.13) \quad \rho_0 \mathbf{u}_t + \nabla p' = -\frac{1}{1-m_0} m' \nabla p' + \frac{1-m_0}{2\rho_0 c^2} \nabla p'^2 - \frac{\rho_0}{2} \nabla (\mathbf{u} \cdot \mathbf{u}) - \frac{\left(\frac{4}{3}\mu + \mu_b\right)}{n_0} \nabla n'_t.$$

2.2.2. Simplifying the conservation of mass equation. Now, let us apply a similar procedure to (2.3). We substitute (2.7) into (2.3) to obtain

$$((1-m)\rho_l)_t + \nabla \cdot ((1-m)\rho_l \mathbf{u}) = 0.$$

The decomposition for the quantities into their mean and fluctuating parts yields

$$\begin{aligned} -\rho_{l0} m'_t + (1-m_0) \rho'_{lt} + (1-m_0) \rho_{l0} \nabla \cdot \mathbf{u} &= \rho'_l m'_t + m' \rho'_{lt} + \rho_{l0} \mathbf{u} \cdot \nabla m' - (1-m_0) \mathbf{u} \cdot \nabla \rho'_l \\ &\quad - (1-m_0) \rho'_l \nabla \cdot \mathbf{u} + \rho_{l0} m' \nabla \cdot \mathbf{u}, \end{aligned}$$

where the first-order terms are on the left hand-side, second-order terms are collected on the right-hand side and higher-order terms have been neglected, similarly to before. By using the linear approximations (2.9)–(2.12), we approximate these terms as follows:

$$\begin{aligned} \rho'_l m'_t &\approx \frac{1}{c^2} p' m'_t, & m' \rho'_{lt} &\approx \frac{1}{c^2} m' p'_t, \\ \rho_{l0} \mathbf{u} \cdot \nabla m' &\approx \frac{\rho_0}{1-m_0} \mathbf{u} \cdot \nabla m', \\ -(1-m_0) \mathbf{u} \cdot \nabla \rho'_l &\approx -\frac{1-m_0}{c^2} \mathbf{u} \cdot \nabla p' = \frac{\rho_0(1-m_0)}{2c^2} (\mathbf{u} \cdot \mathbf{u})_t, \\ -(1-m_0) \rho'_l \nabla \cdot \mathbf{u} &\approx \frac{1-m_0}{c^2} p' \left(\frac{1-m_0}{\rho_0 c^2} p'_t - \frac{1}{1-m_0} m'_t \right) = \frac{(1-m_0)^2}{2\rho_0 c^4} (p'^2)_t - \frac{1}{c^2} p' m'_t, \\ \rho_{l0} m' \nabla \cdot \mathbf{u} &\approx \rho_{l0} m' \left(-\frac{1-m_0}{\rho_0 c^2} p'_t + \frac{1}{1-m_0} m'_t \right) = -\frac{1}{c^2} m' p'_t + \frac{\rho_0}{2(1-m_0)^2} (m'^2)_t. \end{aligned}$$

Altogether, we arrive at

$$(2.14) \quad \begin{aligned} -\frac{\rho_0}{1-m_0}m'_t + (1-m_0)\rho'_{tt} + \rho_0\nabla \cdot \mathbf{u} = & \frac{\rho_0}{(1-m_0)}\mathbf{u} \cdot \nabla m' + \frac{\rho_0(1-m_0)}{2c^2}(\mathbf{u} \cdot \mathbf{u})_t \\ & + \frac{(1-m_0)^2}{2\rho_0c^4}(p'^2)_t + \frac{\rho_0}{2(1-m_0)^2}(m'^2)_t. \end{aligned}$$

By substituting the nonlinear state equation (2.6) into (2.14), we obtain the following approximate version of (2.2):

$$(2.15) \quad \begin{aligned} -\frac{\rho_0}{1-m_0}m'_t + \frac{1-m_0}{c^2}p'_t - \frac{(1-m_0)^2}{\rho_0c^4}\frac{B}{2A}(p'^2)_t - \frac{\gamma(1-m_0)^2}{\rho_0c^4}\left(\frac{1}{c_v} - \frac{1}{c_p}\right)p'_{tt} \\ = -\rho_0\nabla \cdot \mathbf{u} + \frac{(1-m_0)^2}{2\rho_0c^4}(p'^2)_t + \frac{\rho_0}{2(1-m_0)^2}(m'^2)_t \\ + \frac{\rho_0}{1-m_0}\mathbf{u} \cdot \nabla m' + \frac{\rho_0(1-m_0)}{2c^2}(\mathbf{u} \cdot \mathbf{u})_t. \end{aligned}$$

2.2.3. Combining the simplified equations. Analogously to the derivation of nonlinear acoustic models for thermoviscous fluids, we apply the divergence operator to (2.13)

$$(2.16) \quad \begin{aligned} \rho_0(\nabla \cdot \mathbf{u}_t) + \Delta p' = & -\frac{1}{(1-m_0)}\nabla \cdot (m'\nabla p') + \frac{1-m_0}{2\rho_0c^2}\Delta p'^2 \\ & - \frac{\rho_0}{2}\Delta(\mathbf{u} \cdot \mathbf{u}) - \frac{\left(\frac{4}{3}\mu + \mu_b\right)}{n_0}\Delta n'_t \end{aligned}$$

and a time derivative to (2.15)

$$(2.17) \quad \begin{aligned} -\frac{\rho_0}{1-m_0}m'_{tt} + \frac{1-m_0}{c^2}p'_{tt} - \frac{(1-m_0)^2}{\rho_0c^4}\frac{B}{2A}(p'^2)_{tt} - \frac{\gamma(1-m_0)^2}{\rho_0c^4}\left(\frac{1}{c_v} - \frac{1}{c_p}\right)p'_{ttt} \\ = -\rho_0(\nabla \cdot \mathbf{u})_t + \frac{(1-m_0)^2}{2\rho_0c^4}(p'^2)_{tt} + \frac{\rho_0}{2(1-m_0)^2}(m'^2)_{tt} \\ + \frac{\rho_0}{1-m_0}(\mathbf{u} \cdot \nabla m')_t + \frac{\rho_0(1-m_0)}{2c^2}(\mathbf{u} \cdot \mathbf{u})_{tt}. \end{aligned}$$

Subtracting (2.17) from (2.16) leads to the cancellation of the $\rho_0(\nabla \cdot \mathbf{u}_t)$ terms and yields

$$(2.18) \quad \begin{aligned} \Delta p' - \frac{1-m_0}{c^2}p'_{tt} + \frac{\rho_0}{1-m_0}m'_{tt} + \frac{(1-m_0)^2}{\rho_0c^4}\frac{B}{2A}(p'^2)_{tt} \\ + \frac{\gamma(1-m_0)^2}{\rho_0c^4}\left(\frac{1}{c_v} - \frac{1}{c_p}\right)p'_{ttt} - \frac{1-m_0}{2\rho_0c^2}\Delta p'^2 + \frac{(1-m_0)^2}{2\rho_0c^4}(p'^2)_{tt} \\ = -\frac{1}{1-m_0}\nabla \cdot (m'\nabla p') - \frac{\left(\frac{4}{3}\mu + \mu_b\right)}{n_0}\Delta n'_t - \frac{\rho_0}{2}\Delta(\mathbf{u} \cdot \mathbf{u}) - \frac{\rho_0}{2(1-m_0)^2}(m'^2)_{tt} \\ - \frac{\rho_0}{1-m_0}(\mathbf{u} \cdot \nabla m')_t - \frac{\rho_0(1-m_0)}{2c^2}(\mathbf{u} \cdot \mathbf{u})_{tt}. \end{aligned}$$

We next make use of the relation

$$m'_t = \frac{(1-m_0)^2}{\rho_0c^2}p'_t - \frac{1-m_0}{n_0}n'_t$$

that results from subtracting (2.11) from (2.12). Together with (2.10), we obtain

$$-\frac{1}{1-m_0}\nabla \cdot (m'\nabla p') - \frac{\rho_0}{1-m_0}(\mathbf{u} \cdot \nabla m')_t$$

$$\begin{aligned}
&= -\frac{1}{1-m_0}m'\Delta p' - \frac{\rho_0}{1-m_0}\mathbf{u} \cdot \nabla m'_t \\
&= -\frac{1}{1-m_0}m'\Delta p' + \frac{\rho_0(1-m_0)}{c^2}\mathbf{u} \cdot \mathbf{u}_{tt} - \rho_0\mathbf{u} \cdot \Delta\mathbf{u}.
\end{aligned}$$

This approach yields the following replacement for equation (2.18):

$$\begin{aligned}
&\Delta p' - \frac{1-m_0}{c^2}p'_{tt} + \frac{\rho_0}{1-m_0}m'_{tt} + \frac{(1-m_0)^2}{\rho_0 c^4} \frac{B}{2A} (p'^2)_{tt} \\
&\quad + \frac{\gamma(1-m_0)^2}{\rho_0 c^4} \left(\frac{1}{c_v} - \frac{1}{c_p} \right) p'_{ttt} - \frac{(1-m_0)}{2\rho_0 c^2} \Delta p'^2 + \frac{(1-m_0)^2}{2\rho_0 c^4} (p'^2)_{tt} \\
(2.19) \quad &= -\frac{1}{1-m_0}m'\Delta p' + \rho_0\mathbf{u} \cdot \left(\frac{(1-m_0)}{c^2}\mathbf{u}_{tt} - \Delta\mathbf{u} \right) - \frac{(\frac{4}{3}\mu + \mu_b)}{n_0} \Delta n'_t \\
&\quad - \frac{\rho_0}{2} \Delta(\mathbf{u} \cdot \mathbf{u}) - \frac{\rho_0(1-m_0)}{2c^2} (\mathbf{u} \cdot \mathbf{u})_{tt} - \frac{\rho_0}{2(1-m_0)^2} (m'^2)_{tt}.
\end{aligned}$$

Additionally, we use the relations between time and spatial derivatives according to the linear wave equation for pressure and acoustic velocity that are given by

$$(2.20) \quad \Delta p' \approx \frac{1}{c^2}p'_{tt}, \quad \Delta p'^2 \approx \frac{1}{c^2}(p'^2)_{tt},$$

$$(2.21) \quad \Delta\mathbf{u} \approx \frac{1}{c^2}\mathbf{u}_{tt}, \quad \Delta(\mathbf{u} \cdot \mathbf{u}) \approx \frac{1}{c^2}(\mathbf{u} \cdot \mathbf{u})_{tt}.$$

Employing (2.20) and (2.21) within the right-hand side of (2.19) yields

$$\begin{aligned}
&\Delta p' - \frac{1-m_0}{c^2}p'_{tt} + \frac{\rho_0}{1-m_0}m'_{tt} + \frac{(1-m_0)^2}{\rho_0 c^4} \frac{B}{2A} (p'^2)_{tt} + \frac{\gamma(1-m_0)^2}{\rho_0 c^2} \left(\frac{1}{c_v} - \frac{1}{c_p} \right) \Delta p'_t \\
&= -\frac{1}{1-m_0}m'\Delta p' + \frac{(1-m_0)m_0}{2\rho_0 c^4} (p'^2)_{tt} - \frac{(\frac{4}{3}\mu + \mu_b)}{n_0} \Delta n'_t \\
&\quad + \frac{\rho_0 m_0}{c^2} (\mathbf{u} \cdot \mathbf{u})_t - \frac{\rho_0}{c^2} (\mathbf{u} \cdot \mathbf{u})_{tt} - \frac{\rho_0}{2(1-m_0)^2} (m'^2)_{tt}.
\end{aligned}$$

By collecting similar terms, we obtain

$$\begin{aligned}
&\Delta p' - \frac{1-m_0}{c^2}p'_{tt} + \frac{\rho_0}{1-m_0}m'_{tt} + \frac{\tilde{\beta}}{\rho_0 c^4} (p'^2)_{tt} + \frac{b}{c^2} \Delta p'_t \\
(2.22) \quad &= -\frac{1}{1-m_0}m'\Delta p' - \frac{(\frac{4}{3}\mu + \mu_b)}{n_0} \Delta n'_t - \frac{\rho_0}{2(1-m_0)^2} (m'^2)_{tt} \\
&\quad + \frac{\rho_0 m_0}{c^2} (\mathbf{u} \cdot \mathbf{u})_t - \frac{\rho_0}{c^2} (\mathbf{u} \cdot \mathbf{u})_{tt}
\end{aligned}$$

with $b = \frac{\gamma(1-m_0)^2}{\rho_0} \left(\frac{1}{c_v} - \frac{1}{c_p} \right)$ and $\tilde{\beta} = (1-m_0)^2 \frac{B}{2A} - \frac{(1-m_0)m_0}{2}$.

2.2.4. Kuznetsov and Westervelt equations for bubbly fluids. To arrive at bubbly media counterparts of classical models of nonlinear acoustics, we now consider the case that the bubble number density is constant in the equilibrium state, such that $n = n_0$ and hence $m = n_0 v$. Additionally, we assume that the mean volume fraction occupied by gas is negligible ($m_0 \approx 0$), allowing us to approximate $\rho_0 \approx \rho_{l0}$.

- *Nonlinear in v' .* Considering all terms up to second order for p' and $m' = n_0 v$, we can reduce (2.22) to

$$(2.23) \quad \begin{aligned} \frac{1}{c^2} p'_{tt} - \Delta p' - \frac{b}{c^2} \Delta p'_t - \frac{1}{\rho_0 c^4} \frac{B}{2A} (p'^2)_{tt} - \frac{\rho_0}{c^2} (\mathbf{u} \cdot \mathbf{u})_{tt} \\ = \rho_0 n_0 v'_{tt} + n_0 v' \Delta p' + \frac{\rho_0 n_0^2}{2} (v'^2)_{tt} \end{aligned}$$

where $b = \frac{\gamma}{\rho_0} \left(\frac{1}{c_v} - \frac{1}{c_p} \right)$ is the sound diffusivity. This is an inhomogeneous version of the Kuznetsov equation [19] with nonlinear coupling terms on the right-hand side. With the commonly used approximation

$$(2.24) \quad \|\mathbf{u}\| = \sqrt{\mathbf{u} \cdot \mathbf{u}} \approx \left| \frac{1}{c \rho_0} p' \right|$$

(valid if the propagation distance is much larger than a wavelength), we can reduce equation (2.23) to the inhomogeneous Westervelt equation given by

$$(2.25) \quad \frac{1}{c^2} p'_{tt} - \Delta p' - \frac{b}{c^2} \Delta p'_t - \frac{\beta}{\rho_0 c^4} (p'^2)_{tt} = \rho_0 n_0 v'_{tt} + n_0 v' \Delta p' + \frac{\rho_0 n_0^2}{2} (v'^2)_{tt}$$

with $\beta = \frac{B}{2A} + 1$.

- *Linear in v' .* Retaining only first-order terms for $m = n_0 v$ permits further reduction of equation (2.22) to

$$(2.26) \quad \frac{1}{c^2} p'_{tt} - \Delta p' - \frac{b}{c^2} \Delta p'_t - \frac{1}{\rho_0 c^4} \frac{B}{2A} (p'^2)_{tt} - \frac{\rho_0}{c^2} (\mathbf{u} \cdot \mathbf{u})_{tt} = \rho_0 n_0 v'_{tt}.$$

Equation (2.26) is an inhomogeneous Kuznetsov equation with the right-hand side terms that are linear in v' . By employing (2.24) as before, we obtain the following version of the inhomogeneous Westervelt equation:

$$(2.27) \quad \frac{1}{c^2} p'_{tt} - \Delta p' - \frac{b}{c^2} \Delta p'_t - \frac{\beta}{\rho_0 c^4} (p'^2)_{tt} = \rho_0 n_0 v'_{tt},$$

which will be at the focal point of our theoretical and numerical investigations. Observe that equation (2.27) has been derived by taking into account all terms up to second order for p' but retaining only terms that are linear in v' .

2.3. Derivation of acoustic equations in bubbly tissue-like media. We next want to generalize the derived models by introducing fractional derivatives following [29] which allow more accurate modeling of acoustic attenuation in tissue-like media. Therefore, instead of (2.4) we make use of the fractional integral generalization of the conservation of momentum given by

$$(2.28) \quad \rho (\mathbf{u}_t + (\mathbf{u} \cdot \nabla) \mathbf{u}) + \nabla p = \mu \tau_1^{\alpha_1-1} I^{1-\alpha_1} \Delta \mathbf{u} + \left(\frac{\mu}{3} + \mu_b \right) \tau_1^{\alpha_1-1} I^{1-\alpha_1} (\nabla (\nabla \cdot \mathbf{u}))$$

for $0 < \alpha_1 \leq 1$, where τ_1 is a time constant characteristic of the creep time of the medium. Further, $I^{1-\alpha_1}(\cdot)$ represents the fractional integral of order $1 - \alpha_1$ that is defined as follows:

$$I^y[f(t)] = \frac{1}{\Gamma(y)} \int_0^t (t-s)^{y-1} f(s) \, ds \quad \text{for } 0 < y.$$

The fractional integral appearing in (2.28) originates from using a fractional Kelvin–Voigt model for the stress tensor; we refer to [29] for details.

We also make use of the fractional form of the generalized state equation given by

$$(2.29) \quad \rho'_l = \frac{p'}{c^2} - \frac{1}{\rho_{l0}c^4} \frac{B}{2A} p'^2 - \frac{\gamma\tau_2^{\alpha_2-2}}{\rho_{l0}c^4} \left(\frac{1}{c_v} - \frac{1}{c_p} \right) D_t^{\alpha_2-1} p'$$

for $1 < \alpha_2 \leq 2$, where $D_t^{\alpha_2}(\cdot)$ stands for the fractional time derivative of order α_2 that results from having a fractional entropy equation in the medium; see [29]. It is defined as follows:

$$(2.30) \quad D_t^y f(t) = \frac{1}{\Gamma(1-y)} \int_0^t (t-s)^{-y} D_t^n f(s) ds,$$

where $0 \leq n-1 < y < n$, $r = y-n+1$, $n \in \mathbb{N}$; see [18, Sec. 1].

Equations (2.1), (2.3), (2.5), and (2.7) together with the fractional equations (2.28) and (2.29) and an ODE for the bubble radius are a set of seven equations for the seven fluctuations as before. We can then follow the derivation analogously to above by making use of Lighthill's scheme and the substitution corollary combining these equations.

With the approximations above and

$$I^{1-\alpha_1} (\nabla (\nabla \cdot \mathbf{u})) = I^{1-\alpha_1} (\nabla \cdot \nabla \mathbf{u}) = I^{1-\alpha_1} \left(-\frac{1}{n_0} \nabla n'_t \right) = -\frac{1}{n_0} D_t^{\alpha_1} \nabla n',$$

where we have made use of the property

$$D_t^{\alpha_1} [I^{\alpha_2}](\cdot) = \begin{cases} D_t^{\alpha_1-\alpha_2}(\cdot) & \text{if } 0 < \alpha_2 < \alpha_1, \\ I^{\alpha_2-\alpha_1}(\cdot) & \text{if } 0 < \alpha_1 < \alpha_2, \end{cases}$$

we arrive at

$$(2.31) \quad \rho_0 \mathbf{u}_t + \nabla p' = -\frac{1}{1-m_0} m' \nabla p' + \frac{1-m_0}{2\rho_0 c^2} \nabla p'^2 - \frac{\rho_0}{2} \nabla (\mathbf{u} \cdot \mathbf{u}) - \tau_1^{\alpha_1-1} \frac{(\frac{4}{3}\mu + \mu_b)}{n_0} D_t^{\alpha_1} \nabla n'.$$

Substituting the fractional nonlinear state equation (2.28) into (2.14) yields

$$(2.32) \quad \begin{aligned} & -\frac{\rho_0}{1-m_0} m'_t + \frac{1-m_0}{c^2} p'_t - \frac{(1-m_0)^2}{\rho_0 c^4} \frac{B}{2A} (p'^2)_t - \frac{\gamma\tau_2^{\alpha_2-2}(1-m_0)^2}{\rho_0 c^4} \left(\frac{1}{c_v} - \frac{1}{c_p} \right) D_t^{\alpha_2} p' \\ & = \frac{\rho_0}{1-m_0} \mathbf{u} \cdot \nabla m' + \frac{\rho_0(1-m_0)}{2c^2} (\mathbf{u} \cdot \mathbf{u})_t + \frac{(1-m_0)^2}{2\rho_0 c^4} (p'^2)_t + \frac{\rho_0}{2(1-m_0)^2} (m'^2)_t \\ & \quad - \rho_0 \nabla \cdot \mathbf{u}. \end{aligned}$$

Subtracting the time derivative of (2.32) from the divergence of (2.31) yields

$$\begin{aligned} & \Delta p' - \frac{1-m_0}{c^2} p'_{tt} + \frac{\rho_0}{1-m_0} m'_{tt} + \frac{(1-m_0)^2}{\rho_0 c^4} \frac{B}{2A} (p'^2)_{tt} + \frac{\gamma\tau_2^{\alpha_2-2}(1-m_0)^2}{\rho_0 c^4} \left(\frac{1}{c_v} - \frac{1}{c_p} \right) D_t^{\alpha_2+1} p' \\ & = -\frac{1}{1-m_0} \nabla \cdot (m' \nabla p') + \frac{(1-m_0)}{2\rho_0 c^2} \Delta p'^2 - \frac{\rho_0}{2} \Delta (\mathbf{u} \cdot \mathbf{u}) - \tau_1^{\alpha_1-1} \frac{(\frac{4}{3}\mu + \mu_b)}{n_0} \Delta D_t^{\alpha_1} n' \\ & \quad - \frac{\rho_0}{1-m_0} (\mathbf{u} \cdot \nabla m')_t - \frac{\rho_0(1-m_0)}{2c^2} (\mathbf{u} \cdot \mathbf{u})_{tt} - \frac{(1-m_0)^2}{2\rho_0 c^4} (p'^2)_{tt} - \frac{\rho_0}{2(1-m_0)^2} (m'^2)_{tt}. \end{aligned}$$

Analogously to deriving equation (2.22), we obtain

$$(2.33) \quad \begin{aligned} \Delta p' - \frac{1-m_0}{c^2} p'_{tt} + \frac{\rho_0}{1-m_0} m'_{tt} + \frac{\tilde{\beta}}{\rho_0 c^4} (p'^2)_{tt} + \frac{\tau^{\alpha-1} \tilde{b}}{c^2} D_t^\alpha \Delta p' \\ = - \frac{1}{1-m_0} m' \Delta p' - \frac{\tau^{\alpha-1} \left(\frac{4}{3} \mu + \mu_b \right)}{n_0} D_t^\alpha \Delta n' - \frac{\rho_0}{2(1-m_0)^2} (m'^2)_{tt} \\ + \frac{\rho_0 m_0}{c^2} (\mathbf{u} \cdot \mathbf{u})_t - \frac{\rho_0}{c^2} (\mathbf{u} \cdot \mathbf{u})_{tt} \end{aligned}$$

with $\tilde{b} = \frac{\gamma(1-m_0)^2}{\rho_0} \left(\frac{1}{c_v} - \frac{1}{c_p} \right)$ and $\tilde{\beta} = (1-m_0)^2 \frac{B}{2A} - \frac{(1-m_0)m_0}{2}$, where we have linked the fractional derivatives with $\tau = \tau_1 = \tau_2$ by setting $\alpha = \alpha_1 = \alpha_2 - 1$ with $0 < \alpha \leq 1$ since $\alpha_1 = 1$, $\alpha_2 = 2$ leads to (2.22).

2.3.1. Westervelt equation for bubbly tissue media. We can reduce equation (2.33) for different cases analogously to before. We here just state the Westervelt type equation that we focus on in the following sections. By retaining only linear terms for $m = n_0 v$, we arrive at the inhomogeneous Westervelt equation with time-fractional attenuation:

$$(2.34) \quad \frac{1}{c^2} p'_{tt} - \Delta p' - \frac{\tau^{\alpha-1} b}{c^2} D_t^\alpha \Delta p' - \frac{\beta}{\rho_0 c^4} (p'^2)_{tt} = \rho_0 n_0 v'_{tt}$$

with $0 < \alpha \leq 1$, and $b = \frac{\gamma}{\rho_0} \left(\frac{1}{c_v} - \frac{1}{c_p} \right)$ and $\beta = \frac{B}{2A} + 1$ as before.

2.4. Coupling to microbubble dynamics. Solving equations (2.27), (2.25), as well as equation (2.34) with time-fractional dissipation requires an additional relation between the sound pressure and the microbubble volume and we therefore couple it with a type of Rayleigh–Plesset equation in terms of the bubble radius R together with the volume–radius relation

$$v = \frac{4}{3} \pi R^3.$$

2.4.1. Overview of models of microbubble dynamics. As already mentioned, many different models exist for describing the oscillating dynamics of microbubbles. We provide an overview here and refer to, e.g., the book [5] and the review papers [8, 32] for further details. Starting from

$$\rho \left[R R_{tt} + \frac{3}{2} R_t^2 \right] = p_{\text{int}} - p_{\text{ext}}$$

where we recall that ρ is the mass density of the medium and p_{int} the internal pressure, the simplest Rayleigh–Plesset equation is given by

$$(2.35) \quad \rho \left[R R_{tt} + \frac{3}{2} R_t^2 \right] = p_v - p_{\text{stat}} - 4\mu \frac{R_t}{R} - p'$$

In (2.35), p_v denotes the vapor pressure, and p_{stat} is the static ambient pressure. Furthermore, μ in (2.37) is the viscosity of the (tissue) medium. We introduce

$$p_b = p_v - p_{\text{stat}},$$

so that (2.35) becomes

$$(2.36) \quad \rho \left[R R_{tt} + \frac{3}{2} R_t^2 \right] = p_b - 4\mu \frac{R_t}{R} - p'.$$

A modified Rayleigh–Plesset equation is given by

$$(2.37) \quad \rho \left[R R_{tt} + \frac{3}{2} R_t^2 \right] = p_b - 4\mu \frac{R_t}{R} - \frac{2\sigma}{R} - p'.$$

The coefficient σ (2.37) is the surface tension between the liquid and vapor/gas at the bubble wall; see Figure 1.

A further extension of the ODE arises from taking bubble contents into considerations. A generalized Rayleigh–Plesset equation, also known as the RPNNP (which stands for Rayleigh–Plesset–Noltingk–Neppiras–Poritsky) equation is given by

$$(2.38) \quad \rho \left[RR_{tt} + \frac{3}{2} R_t^2 \right] = p_b - 4\mu \frac{R_t}{R} - \frac{2\sigma}{R} + p_{pgn} \left(\frac{R_0}{R} \right)^{3\kappa} - p';$$

see [27, 30]. Here p_{pgn} is the (constant) gas pressure inside the bubble at rest given by

$$p_{pgn} = \frac{2\sigma}{R_0} - p_b;$$

see [21]. Furthermore, R_0 in (2.38) is the equilibrium radius, i.e., the radius of a bubble at rest and $\kappa \geq 1$ is the adiabatic index; see Figure 1.

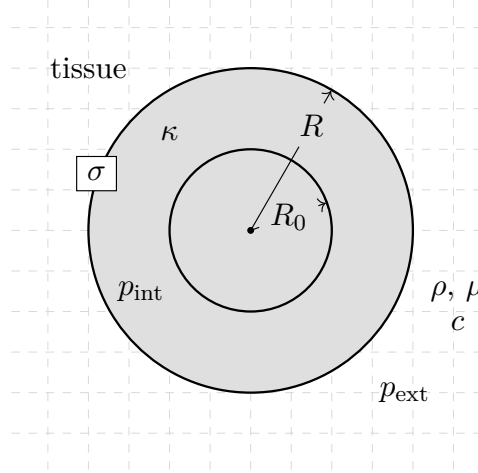


FIGURE 1. Single-microbubble dynamics; figure adapted from [21]

- *Incorporating acoustic radiation.* Other versions of microbubble models arise from considering damping of the bubble dynamics by the sound radiated by the bubble. A model that incorporates sound radiation is given by

$$(2.39) \quad \rho \left[RR_{tt} + \frac{3}{2} R_t^2 \right] = p_b - 4\mu \frac{R_t}{R} - \frac{2\sigma}{R} + p_{pgn} \left(\frac{R_0}{R} \right)^{3\kappa} \left(1 - 3\kappa \frac{R_t}{c} \right) - p';$$

see [32].

- *Coated-bubble dynamics.* The coating of bubbles is known to stabilize them and prolong their existence; see, e.g., [32]. In this case, the size-dependent effective surface tension can given by

$$(2.40) \quad \sigma(R) = \chi \left(\frac{R^2}{R_0^2} - 1 \right),$$

where χ is the shell elasticity. The dynamics of microbubbles with thin shells can then be described by

$$(2.41) \quad \rho \left[RR_{tt} + \frac{3}{2} R_t^2 \right] = p_b - 4\mu \frac{R_t}{R} - \frac{2\sigma(R)}{R} + p_{pgn} \left(\frac{R_0}{R} \right)^{3\kappa} \left(1 - 3\kappa \frac{R_t}{c} \right) - 4\kappa_s \frac{R_t}{R^2} - p'$$

with

$$p_{\text{pgn}} = \frac{2\sigma_0}{R_0} - p_b,$$

where σ_0 is the surface tension of the bubble at rest and κ_s is the surface dilatational viscosity of the shell; see [32, eq. (8)]. Further models that take the width of the shell into account can be found in, e.g., [26, Appendix A] and the review paper [8].

2.5. Westervelt–Rayleigh–Plesset system. Going forward, in the analysis, we consider the following mathematically generalized equation for the dynamics of microbubbles:

$$\rho \left[RR_{tt} + \frac{3}{2} R_t^2 \right] = h_0(R, R_t) - p',$$

where we impose local Lipschitz continuity on the function h_0 ; see Theorems 3.1 and 3.2 for details. The assumptions allow having

$$(2.42) \quad h_0(R, R_t) = p_b - \frac{4\mu}{R} R_t - \frac{2\sigma(R)}{R} + p_{\text{pgn}} \left(\frac{R_0}{R} \right)^{3\kappa} \left(1 - 3\kappa_0 \frac{R_t}{c} \right) - 4\kappa_s \frac{R_t}{R^2}$$

with σ constant or given by (2.40) and $\kappa_s, \kappa_0 \in \mathbb{R}$ so that (2.39) (with $\kappa_0 = \kappa$) and the simpler model in (2.38) (with $\kappa_0 = \kappa_s = 0$) are covered by our theoretical results. The equation is coupled with the damped Westervelt equation for the pressure:

$$((1 + 2k(x)p')p'_t)_t - c^2 \Delta p' + \mathcal{A}p' = \frac{4}{3}\pi c^2 \eta (R^3)_{tt},$$

where $\eta = \rho_0 n_0$ and the attenuation operator is given either by $\mathcal{A}p' = -b\Delta p'_t$ or $\mathcal{A}p' = -b\tau^{\alpha-1} \Delta D_t^\alpha p'$ for $\alpha \in (0, 1)$. Above we have used the fact that $v'_{tt} = v_{tt}$ to arrive at the right-hand side of the equation. When considering this coupled system, $R = R(x, t)$ is a function of both time and space. Thus, the equation governing the dynamics of microbubbles is an ODE defined pointwise in space.

Remark 1 (On other coupled models for bubbly liquids). *Another model for bubbly liquids that is based on the assumption that bubbles provide the dominant source of nonlinearity is presented in [10, Ch. 5]. It consists of the inhomogeneous linear wave equation for the pressure:*

$$(2.43) \quad p'_{tt} - c^2 \Delta p' = c^2 \eta v_{tt}$$

together with an ODE in terms of the volume v for the dynamics of microbubbles:

$$(2.44) \quad v_{tt} + \delta \frac{4\mu}{R_0^2} v_t + \omega_0^2 v + \frac{4\pi R_0}{\rho_0} p = \frac{(\kappa + 1)\omega_0^2}{2v_0} v^2 + \frac{1}{6v_0} (2vv_{tt} + v_t^2)$$

where $\omega_0^2 = \frac{3\kappa p_0}{\rho_0 R_0^2}$. In the absence of nonlinearity, which means neglecting the terms on the right-hand side, equation (2.44) describes the forced response of a harmonic oscillator with an undamped natural frequency ω_0 . This equation approximates equation (2.36) up to second order in v , using the relation $v = \frac{4}{3}\pi R^3$ and the adiabatic gas law $\frac{p_b}{p_0} = \left(\frac{v_0}{v} \right)^\kappa$. This transformation removes the singularity and simplifies the ODE, but also results in the loss of certain effects as it involves a further approximation. Wave equation (2.43) can be obtained from the Westervelt equation by setting $k = k(x)$ and b to zero. However, this reduction also means that the complex, nonlinear effects of high-intensity ultrasound fields are not captured. The Westervelt–Rayleigh–Plesset model can be seen as a more comprehensive model, accounting for a broader range of effects arising from both bubble dynamics and the ultrasound field.

3. ANALYSIS OF THE WESTERVELT–RAYLEIGH–PLESSET SYSTEM

In this section, we analyze the Westervelt–Rayleigh–Plesset system. For simplicity of notation, we drop $(\cdot)'$ when denoting fluctuating pressure quantities and use p instead of p' , but we keep the notation $R = R_0 + R'$ for the total bubble radius. We consider the following initial boundary-value problem:

$$(3.1) \quad \begin{cases} ((1 + 2k(x)p)p_t)_t - c^2 \Delta p + \mathcal{A}p = \xi(R^3)_{tt} & \text{in } \Omega \times (0, T), \\ (p, p_t)|_{t=0} = (p_0, p_1), \quad p|_{\partial\Omega} = 0, \\ \rho \left[RR_{tt} + \frac{3}{2} R_t^2 \right] = h_0(R, R_t) - p & \text{in } \Omega \times (0, T), \\ (R, R_t)|_{t=0} = (R_0, R_1), \end{cases}$$

with $\xi \in \mathbb{R}$ (corresponding to $\frac{4}{3}\pi c^2 \eta$ in the derivation) and acoustic dissipation is given either by $\mathcal{A}p = -b\Delta p_t$ or $\mathcal{A}p = -br^{\alpha-1} \Delta D_t^\alpha p$, where $\alpha \in (0, 1)$. The aim of this section is to determine the conditions on the initial pressure-bubble data under which (3.1) has a unique solution. As the two cases of acoustic dissipation allow for different assumptions on the data and variable coefficient k (being that strong dissipation leads to parabolic-like acoustic evolution), we treat them separately.

Notation in this section. Below we use $x \lesssim y$ to denote $x \leq Cy$, where $C > 0$ is a generic positive constant. We employ the following notation for Sobolev spaces on smooth domains equipped with boundary conditions:

$$H_\diamondsuit^2(\Omega) = H^2(\Omega) \times H_0^1(\Omega), \quad H_\diamondsuit^3(\Omega) = \{p \in H^3(\Omega) : p|_{\partial\Omega} = \Delta p|_{\partial\Omega} = 0\}.$$

When denoting norms in Bochner spaces, we omit the temporal domain; for example, $\|\cdot\|_{L^p(L^q(\Omega))}$ denotes the norm in $L^p(0, T; L^q(\Omega))$.

3.1. The Westervelt–Rayleigh–Plesset system with strong acoustic attenuation. We recall first a well-posedness result for the Westervelt equation for non-bubbly media with strong attenuation, which is needed to set up the analysis of the coupled problem. This form of Westervelt's equation has been extensively studied in the mathematical literature; see, e.g., [12, 14, 16, 24] and the references provided therein. One of the key aspects of its analysis is ensuring that the factor $1 + 2kp$ next to the second time derivative of the pressure stays positive (i.e., that it does not degenerate), which can be achieved through sufficiently small (and smooth) data.

Proposition 3.1. *Assume that $\Omega \subset \mathbb{R}^d$, $d \in \{1, 2, 3\}$ is a bounded and $C^{1,1}$ -regular domain. Let $c, b > 0$ and $k \in L^\infty(\Omega)$. Furthermore, let*

$$(p_0, p_1) \in H_\diamondsuit^2(\Omega) \times H_0^1(\Omega) \quad \text{and} \quad f \in L^2(0, T; L^2(\Omega)).$$

There exists data size $\delta = \delta(T) > 0$, such that if

$$(3.2) \quad \|p_0\|_{H^2(\Omega)} + \|p_1\|_{H^1(\Omega)} + \|f\|_{L^2(L^2(\Omega))} \leq \delta,$$

then there is a unique solution of

$$\begin{cases} ((1 + 2k(x)p)p_t)_t - c^2 \Delta p - b\Delta p_t = f(x, t) & \text{in } \Omega \times (0, T), \\ p|_{\partial\Omega} = 0, \\ (p, p_t)|_{t=0} = (p_0, p_1) \end{cases}$$

in

$$(3.3) \quad X_p = L^\infty(0, T; H_\diamondsuit^2(\Omega)) \cap W^{1,\infty}(0, T; H_0^1(\Omega)) \cap H^2(0, T; L^2(\Omega)),$$

such that

$$1 + 2kp \geq \gamma > 0 \quad \text{in } \Omega \times (0, T)$$

for some $\gamma > 0$. Furthermore, the solution satisfies the following bound:

$$\|p\|_{X_p}^2 \lesssim C(T) \left(\|p_0\|_{H^2(\Omega)}^2 + \|p_1\|_{H^1(\Omega)}^2 + \|f\|_{L^2(L^2(\Omega))}^2 \right).$$

Proof. The proof follows analogously to that of [16, Proposition 1]; the only difference is that here smallness of data is imposed instead of the smallness of $\|k\|_{L^\infty(\Omega)}$. We thus omit the details. \square

Under the assumptions of Proposition 3.1, we can define the solution mapping

$$\mathcal{S} : L^2(0, T; L^2(\Omega)) \rightarrow X_p, \quad \text{such that } \mathcal{S}(f) = p,$$

which will be employed in the analysis of the coupled problem. We will furthermore exploit Lipschitz continuity of this mapping in the following sense. Let $f_1, f_2 \in L^2(0, T; L^2(\Omega))$ and denote $p^{(1)} = \mathcal{S}(f_1)$ and $p^{(2)} = \mathcal{S}(f_2)$. By Proposition 3.1,

$$\|p^{(1)}\|_{X_p}, \|p^{(2)}\|_{X_p} \leq \mathcal{C}$$

for some $\mathcal{C} > 0$. Then it can be shown by considering the equation solved by $p^{(1)} - p^{(2)}$ (analogously to the proof of contractivity in [16, Proposition 1]) that

$$(3.4) \quad \|p^{(1)} - p^{(2)}\|_{X_p} \leq C(T, \mathcal{C}) \|f_1 - f_2\|_{L^2(L^2(\Omega))}.$$

For completeness, the derivation of the above bound is provided in Lemma A.1 in the appendix.

We approach the analysis of the Westervelt–Rayleigh–Plesset system by employing Banach's fixed-point theorem. To this end, we linearize the Rayleigh–Plesset equation, in the general spirit of [3, 33], while eliminating p via the mapping \mathcal{S} . More precisely, to analyze (3.1) with $\mathcal{A}p = -b\Delta p_t$, under the assumptions of Proposition 3.1, we set up the fixed-point mapping

$$\mathcal{T} : \mathcal{B}_R \ni R^* \mapsto R,$$

where R solves the problem

$$(3.5) \quad \begin{cases} R_{tt} = h(R^*, R_t^*, \mathcal{S}(f(R^*))) \\ (R, R_t)|_{t=0} = (R_0, R_1), \end{cases}$$

with $f(R^*) = \xi ((R^*)^3)_{tt}$ and the function h given by

$$(3.6) \quad h(R^*, R_t^*, \mathcal{S}(f(R^*))) = \frac{1}{R^*} \left(-\frac{3}{2}(R_t^*)^2 + \frac{1}{\rho} h_0(R^*, R_t^*) - \frac{1}{\rho} \mathcal{S}(f(R^*)) \right).$$

Above, R^* is taken from the set

$$(3.7) \quad \begin{aligned} \mathcal{B}_R = \{R^* \in C^2([0, T]; L^\infty(\Omega)) : & \|R_{tt}^*\|_{C(L^\infty(\Omega))} \leq M, \\ & \|R^*\|_{C(L^\infty(\Omega))} + \|R_t^*\|_{C(L^\infty(\Omega))} \leq m, \\ & \|R^* - R_0\|_{C(L^\infty(\Omega))} \leq \varepsilon_0, \quad (R^*, R_t^*)|_{t=0} = (R_0, R_1) \}. \end{aligned}$$

In (3.7), $\varepsilon_0 > 0$ is small enough and will be set by the upcoming proof, together with small enough $m > 0$ and an adequately calibrated $M > 0$. We note that the ε_0 condition in (3.7) is there to ensure positivity of the radius of the microbubbles, provided R_0 is positive.

We make the following assumptions on the function h_0 in (3.6). We assume that for any $R^* \in \mathcal{B}_R$,

$$(3.8) \quad \|h_0(R^*, R_t^*)\|_{C(L^\infty(\Omega))} \leq C(m, \varepsilon_0).$$

Furthermore, for any $R^{(1),*}, R^{(2),*} \in \mathcal{B}_R$,

$$(3.9) \quad \|h_0(R^{(1),*}, R_t^{(1),*}) - h_0(R^{(2),*}, R_t^{(2),*})\|_{C(L^\infty(\Omega))} \lesssim \|R^{(1),*} - R^{(2),*}\|_{C^1(L^\infty(\Omega))}.$$

We note that function h_0 in (2.42) satisfies these assumptions; the result is provided in Lemma A.3 in the appendix. We are now ready to prove the first main theoretical result.

Theorem 3.1. *Assume that $\Omega \subset \mathbb{R}^d$, where $d \in \{2, 3\}$, is a bounded and $C^{1,1}$ -regular domain. Furthermore, assume that $c, b > 0$, $\rho > 0$, $\xi \in \mathbb{R}$, and $k \in L^\infty(\Omega)$, and let*

$$(p_0, p_1) \in H_\diamond^2(\Omega) \times H_0^1(\Omega), \quad (R_0, R_1) \in L^\infty(\Omega) \times L^\infty(\Omega),$$

where

$$R_0(x) \geq \underline{R}_0 > 0 \quad \text{a.e. in } \Omega.$$

Let assumptions (3.8) and (3.9) on the function h_0 hold. Then there exist pressure data size $\delta_p > 0$, bubble data size δ_R , and final time \tilde{T} , such that if

$$\|p_0\|_{H^2(\Omega)} + \|p_1\|_{H^1(\Omega)} \leq \delta_p, \quad \|R_0\|_{L^\infty(\Omega)} + \|R_1\|_{L^\infty(\Omega)} \leq \delta_R, \quad \text{and } T \leq \tilde{T},$$

there is a unique $(p, R) \in X_p \times \mathcal{B}_R$ that solves (3.1) with $\mathcal{A}p = -b\Delta p_t$, with X_p defined in (3.3).

Proof. As announced, we carry out the proof by relying on the Banach fixed-point theorem. Note that $\mathcal{B}_R \neq \emptyset$ since the solution of

$$R_{tt} = 0, \quad (R, R_t)|_{t=0} = (R_0, R_1)$$

belongs to \mathcal{B}_R as long as the final time and δ_R are small enough.

Let $R^* \in \mathcal{B}_R$. For small enough $\varepsilon_0 = \varepsilon_0(\underline{R}_0)$, R^* is bounded and positive:

$$(3.10) \quad 0 < \underline{R} := \underline{R}_0 - \varepsilon_0 \leq R_0 - \varepsilon_0 \leq R^*(x, t) \leq \|R_0\|_{L^\infty(\Omega)} + \varepsilon_0 := \overline{R}$$

a.e. in $\Omega \times (0, T)$. Toward checking the assumptions of Proposition 3.1, we note that

$$(3.11) \quad \begin{aligned} & \|f(R^*)\|_{L^2(L^2(\Omega))} \\ &= \xi \|3(R^*)^2 R_{tt}^* + 6R^*(R_t^*)^2\|_{L^2(L^2(\Omega))} \\ &\leq 3\xi \|R^*\|_{C(L^\infty(\Omega))}^2 \sqrt{T} \|R_{tt}^*\|_{C(L^2(\Omega))} + 6\xi \|R^*\|_{C(L^\infty(\Omega))} \sqrt{T} \|R_t^*\|_{C(L^2(\Omega))}^2 \\ &\leq \sqrt{T} C(\Omega) (M + m) m^2. \end{aligned}$$

Therefore, the smallness condition (3.2) can be fulfilled by making δ_p and T small enough so that

$$\delta_p + \sqrt{T} C(\Omega) (M + m) m^2 \leq \delta.$$

Thus, by Proposition 3.1, the mapping \mathcal{S} is well-defined (and, in turn, problem (3.5)) and we have $p = \mathcal{S}(f(R^*))$.

The remainder of the proof is dedicated to showing that \mathcal{T} is a strictly contractive self-mapping.

The self-mapping property: From (3.5), we have the following bound:

$$(3.12) \quad \|R_{tt}\|_{C(L^\infty(\Omega))} \leq \|h(R^*, R_t^*, \mathcal{S}(f(R^*)))\|_{C(L^\infty(\Omega))}.$$

To estimate the h term further, we use the lower bound for R^* established in (3.10):

$$\begin{aligned} & \|h(R^*, R_t^*, \mathcal{S}(f(R^*)))\|_{C(L^\infty(\Omega))} \\ &\leq \frac{1}{\overline{R}} \left\| -\frac{3}{2}(R_t^*)^2 + \frac{1}{\rho} h_0(R^*, R_t^*) - \frac{1}{\rho} \mathcal{S}(f(R^*)) \right\|_{C(L^\infty(\Omega))}. \end{aligned}$$

On account of the fact that $R^* \in \mathcal{B}_R$ and assumption (3.8) made on h_0 , we then have

$$(3.13) \quad \|h(R^*, R_t^*, \mathcal{S}(f(R^*)))\|_{C(L^\infty(\Omega))} \lesssim \|R_t^*\|_{L^\infty(\Omega)}^2 + C(m, \varepsilon_0) + \|\mathcal{S}(f(R^*))\|_{C(L^\infty(\Omega))}.$$

To estimate the \mathcal{S} term, we employ Proposition 3.1 and the embedding $C([0, T]; L^\infty(\Omega)) \hookrightarrow X_p$:

$$\begin{aligned} \|\mathcal{S}(f(R^*))\|_{C(L^\infty(\Omega))} &\leq C(\Omega) \|\mathcal{S}(f(R^*))\|_{X_p} \\ &\leq C(\Omega, T) (\|p_0\|_{H^2(\Omega)} + \|p_1\|_{H^1(\Omega)} + \|f(R^*)\|_{L^2(L^2(\Omega))}). \end{aligned}$$

Then taking into account the bound on f derived in (3.11) yields

$$(3.14) \quad \|\mathcal{S}(f(R^*))\|_{C(L^\infty(\Omega))} \leq C(\Omega, T) (\delta_p + \sqrt{T}(M + m)m^2).$$

Therefore, by employing (3.14) in (3.13) and then (3.12), we conclude that

$$\|R_{tt}\|_{C(L^\infty(\Omega))} \lesssim 1 + \delta_p + m^2 + \sqrt{T}(M + m)m^2 \leq M,$$

provided $M > 0$ is large enough and $T > 0$ small enough relative to it.

Next, we can guarantee that

$$\|R\|_{C(L^\infty(\Omega))} + \|R_t\|_{C(L^\infty(\Omega))} \leq m$$

by possibly further reducing δ_R and T . Indeed, since

$$(3.15) \quad \begin{aligned} R_t &= R_1 + \int_0^t h(R^*, R_t^*, \mathcal{S}(f(R^*))(s) \, ds, \\ R &= R_0 + R_1 t + \int_0^t \int_0^s h(R^*, R_t^*, \mathcal{S}(f(R^*))(\tilde{s}) \, d\tilde{s} \, ds, \end{aligned}$$

we find that that

$$\begin{aligned} &\|R\|_{C(L^\infty(\Omega))} + \|R_t\|_{C(L^\infty(\Omega))} \\ &\leq \|R_0\|_{L^\infty(\Omega)} + (1 + T) \|R_1\|_{L^\infty(\Omega)} + (T + T^2) \|h(R^*, R_t^*, \mathcal{S}(f(R^*)))\|_{C(L^\infty(\Omega))} \\ &\lesssim (1 + T) \delta_R + (T + T^2) [1 + m^2 + \delta_p + \sqrt{T}(M + m)m^2], \end{aligned}$$

which can be made smaller than m by decreasing δ_R and T . To conclude that $R \in \mathcal{B}_R$, it remains to estimate $R - R_0$. To this end, we use the expression for R in (3.15), which yields

$$\|R - R_0\|_{C(L^\infty(\Omega))} \leq T \|R_1\|_{L^\infty(\Omega)} + T^2 \|h(R^*, R_t^*, \mathcal{S}(f(R^*)))\|_{C(L^\infty(\Omega))}.$$

Therefore, reducing T allows us to also conclude that $\|R - R_0\|_{C(L^\infty(\Omega))} \leq \varepsilon_0$, and, in turn, $R \in \mathcal{B}_R$.

Strict contractivity: To prove strict contractivity of \mathcal{T} , we take $R^{(1),*}, R^{(2),*} \in \mathcal{B}_R$ and note that the difference $\bar{\mathcal{R}} = \mathcal{T}(R^{(1),*}) - \mathcal{T}(R^{(2),*})$ solves

$$\bar{\mathcal{R}}_{tt} = h(R^{(1),*}, R_t^{(1),*}, \mathcal{S}(f(R^{(1),*}))) - h(R^{(2),*}, R_t^{(2),*}, \mathcal{S}(f(R^{(2),*})))$$

with zero initial conditions. Thus we immediately have

$$(3.16) \quad \begin{aligned} &\|\bar{\mathcal{R}}\|_{C^2(L^\infty(\Omega))} \\ &\lesssim (1 + T + T^2) \|h(R^{(1),*}, R_t^{(1),*}, \mathcal{S}(f(R^{(1),*}))) - h(R^{(2),*}, R_t^{(2),*}, \mathcal{S}(f(R^{(2),*})))\|_{C(L^\infty(\Omega))}. \end{aligned}$$

We can estimate the difference of h terms further by exploiting the local Lipschitz continuity of h_0 and p to arrive at

$$(3.17) \quad \begin{aligned} &\|h(R^{(1),*}, R_t^{(1),*}, \mathcal{S}(f(R^{(1),*}))) - h(R^{(2),*}, R_t^{(2),*}, \mathcal{S}(f(R^{(2),*})))\|_{C(L^\infty(\Omega))} \\ &\leq \sqrt{T} \cdot C(\underline{R}, \bar{R}, m, M, \tilde{T}) \|\bar{\mathcal{R}}^*\|_{C^2(L^\infty(\Omega))}, \end{aligned}$$

where $\overline{\mathcal{R}}^* = R^{(1),*} - R^{(2),*}$. Indeed, we can rewrite the difference of h terms as follows:

$$\begin{aligned}
 & h(R^{(1),*}, R_t^{(1),*}, \mathcal{S}(f(R^{(1),*}))) - h(R^{(2),*}, R_t^{(2),*}, \mathcal{S}(f(R^{(2),*}))) \\
 &= -\frac{\overline{\mathcal{R}}^*}{R^{(1),*}R^{(2),*}} \left[-\frac{3}{2}(R_t^{(1),*})^2 + \frac{1}{\rho}h_0(R^{(1),*}, R_t^{(1),*}) \right] \\
 (3.18) \quad &+ \frac{1}{R^{(2),*}} \left[-\frac{3}{2}\overline{\mathcal{R}}_t^*(R_t^{(1),*} + R_t^{(2),*}) + \frac{1}{\rho}h_0(R^{(1),*}, R_t^{(1),*}) - \frac{1}{\rho}h_0(R^{(2),*}, R_t^{(2),*}) \right] \\
 &+ \frac{\overline{\mathcal{R}}^*}{\rho R^{(1),*}R^{(2),*}} \mathcal{S}(f(R^{(2),*})) - \frac{1}{\rho R^{(1),*}} (\mathcal{S}(f(R^{(1),*})) - \mathcal{S}(f(R^{(2),*}))) .
 \end{aligned}$$

Thanks to the Lipschitz continuity of the pressure field stated in (3.4) and the embedding $C([0, T]; L^\infty(\Omega)) \hookrightarrow X_p$, we know that

$$\begin{aligned}
 \|\mathcal{S}(f(R^{(1),*})) - \mathcal{S}(f(R^{(2),*}))\|_{C(L^\infty(\Omega))} &\lesssim \|f(R^{(1),*}) - f(R^{(2),*})\|_{L^2(L^2(\Omega))} \\
 &\lesssim \sqrt{T} \|f(R^{(1),*}) - f(R^{(2),*})\|_{C(L^\infty(\Omega))} .
 \end{aligned}$$

We can further see the difference of f terms as

$$\begin{aligned}
 & f(R^{(1),*}) - f(R^{(2),*}) \\
 &= 3\xi [(R^{(1),*})^2 R_{tt}^{(1),*} - (R^{(2),*})^2 R_{tt}^{(2),*}] + 6\xi [R^{(1),*}(R_t^{(1),*})^2 - R^{(2),*}(R_t^{(2),*})^2] \\
 &= 3\xi [\overline{\mathcal{R}}^*(R^{(1),*} + R^{(2),*})R_{tt}^{(1),*} + (R^{(2),*})^2 \overline{\mathcal{R}}_{tt}^*] + 6\xi [\overline{\mathcal{R}}^*(R_t^{(1),*})^2 + R^{(2),*} \overline{\mathcal{R}}_t^*(R_t^{(1),*} + R_t^{(2),*})] .
 \end{aligned}$$

From here, using the fact that $R^{(1),*}, R^{(2),*} \in \mathcal{B}_R$, we obtain

$$\|f(R^{(1),*}) - f(R^{(2),*})\|_{C(L^\infty(\Omega))} \leq C(M)m \|\overline{\mathcal{R}}^*\|_{C^2(L^\infty(\Omega))} .$$

Combining this bound with the continuity of h_0 in the sense of

$$\begin{aligned}
 \|h_0(R^{(1),*}, R_t^{(1),*}) - h_0(R^{(2),*}, R_t^{(2),*})\|_{C(L^\infty(\Omega))} &\lesssim \|R^{(1),*} - R^{(2),*}\|_{C^1(L^\infty(\Omega))} \\
 &\lesssim (T^2 + T) \|R_{tt}^{(1),*} - R_{tt}^{(2),*}\|_{C(L^\infty(\Omega))} ,
 \end{aligned}$$

and estimating the remaining terms on the right-hand side of (3.18) in a similar manner leads to (3.17). Then using (3.17) in (3.16) yields

$$\|\overline{\mathcal{R}}\|_{C^2(L^\infty(\Omega))} \lesssim \sqrt{T} \|\overline{\mathcal{R}}^*\|_{C^2(L^\infty(\Omega))} .$$

Therefore, the mapping \mathcal{T} is strictly contractive with respect to the norm in $C^2([0, T]; L^\infty(\Omega))$ provided final time T is sufficiently small. An application of Banach's fixed-point theorem yields the desired result. \square

3.2. The Westervelt–Rayleigh–Plesset system with time-fractional acoustic attenuation. We next wish to adapt the previous arguments to analyze (3.1) with $\mathcal{A}p = -b\tau^{\alpha-1} \Delta D_t^\alpha p$, where $\alpha \in (0, 1)$. Without loss of generality, we set the relaxation parameter to $\tau = 1$ in this section. We recall first a well-posedness result from [15] on the Westervelt equation in non-bubbly media with time-fractional damping. As the one cannot exploit much of acoustic dissipation in this setting, more smoothness is needed from the data and the variable coefficient k compared to Proposition 3.1.

Proposition 3.2 (see Theorem 3.1 in [15]). *Assume that $\Omega \subset \mathbb{R}^d$, $d \in \{1, 2, 3\}$ is a bounded and $C^{2,1}$ -regular domain. Let $c, b > 0$, and $\alpha \in (0, 1)$. Furthermore, let $k \in W^{1,\infty}(\Omega) \cap W^{2,4}(\Omega)$,*

$$(p_0, p_1) \in H_\diamondsuit^3(\Omega) \times H_\diamondsuit^2(\Omega), \quad \text{and} \quad f \in L^2(0, T; H_\diamondsuit^2(\Omega)) .$$

There exists data size $\tilde{\delta} = \tilde{\delta}(T) > 0$, such that if

$$(3.19) \quad \|p_0\|_{H^3(\Omega)} + \|p_1\|_{H^2(\Omega)} + \|f\|_{L^2(H^2(\Omega))} \leq \tilde{\delta},$$

then there is a unique solution of

$$\begin{cases} ((1 + 2k(x)p)p_t)_t - c^2 \Delta p - b \Delta D_t^\alpha p = f(x, t) & \text{in } \Omega \times (0, T), \\ p|_{\partial\Omega} = 0, \\ (p, p_t)|_{t=0} = (p_0, p_1) \end{cases}$$

in

$$(3.20) \quad \mathfrak{X}_p = L^\infty(0, T; H_\diamond^3(\Omega)) \cap W^{1,\infty}(0, T; H_\diamond^2(\Omega)) \cap H^2(0, T; H_0^1(\Omega))$$

such that

$$1 + 2kp \geq \gamma > 0 \quad \text{in } \Omega \times (0, T)$$

for some $\gamma > 0$. Furthermore, the solution satisfies the following bound:

$$\|p\|_{\mathfrak{X}_p}^2 \lesssim C(T) \left(\|p_0\|_{H^3(\Omega)}^2 + \|p_1\|_{H^2(\Omega)}^2 + \|f\|_{L^2(H^2(\Omega))}^2 \right).$$

Under the assumptions of Proposition 3.2, we can similarly to before introduce the mapping $\mathfrak{S} : L^2(0, T; H_\diamond^2(\Omega)) \rightarrow \mathfrak{X}_p$, such that $\mathfrak{S}(f) = p$. Here, however Lipschitz continuity can only be established in a norm lower than that corresponding to the solution space. Let $f_1, f_2 \in L^2(0, T; H_\diamond^2(\Omega))$ and denote $p^{(1)} = \mathfrak{S}(f_1)$ and $p^{(2)} = \mathfrak{S}(f_2)$. Then it can be shown that

$$(3.21) \quad \|p^{(1)} - p^{(2)}\|_{C^1(L^2(\Omega))} + \|p^{(1)} - p^{(2)}\|_{C(H^1(\Omega))} \lesssim \|f_1 - f_2\|_{L^2(L^2(\Omega))}.$$

For completeness, we provide the proof of this estimate in Lemma A.2 in the appendix.

To analyze the Westervelt–Rayleigh–Plessel system with time-fractional acoustic attenuation, we introduce the fixed-point mapping

$$\mathfrak{T} : \mathfrak{B}_R \ni R^* \mapsto R,$$

which maps R^* taken from the set

$$(3.22) \quad \begin{aligned} \mathfrak{B}_R = \{R^* \in C^2(0, T; H_\diamond^2(\Omega)) : & \|R_{tt}^*\|_{C(H^2(\Omega))} \leq M, \\ & \|R^*\|_{C(H^2(\Omega))} + \|R_t^*\|_{C(H^2(\Omega))} \leq m, \\ & \|R^* - R_0\|_{C([0, T]; L^\infty(\Omega))} \leq \varepsilon_0, \quad (R^*, R_t^*)|_{t=0} = (R_0, R_1) \} \end{aligned}$$

to the solution of

$$\begin{cases} R_{tt} = h(R^*, R_t^*, \mathfrak{S}(f(R^*))), \\ (R, R_t)|_{t=0} = (R_0, R_1). \end{cases}$$

Compared to (3.7), the main difference is the spatial regularity $H^2(\Omega)$ in (3.22), which originates from the need to have the acoustic right-hand side in $L^2(0, T; H_\diamond^2(\Omega))$ as opposed to $L^2(0, T; L^2(\Omega))$. We assume that h is given by (3.6), where h_0 satisfies the following assumptions. For any $R^* \in \mathfrak{B}_R$,

$$(3.23) \quad \|h_0(R^*, R_t^*)\|_{C(H^2(\Omega))} \leq C(m, \varepsilon_0).$$

Furthermore, for any $R^{(1),*}, R^{(2),*} \in \mathfrak{B}_R$,

$$(3.24) \quad \|h_0(R^{(1),*}, R_t^{(1),*}) - h_0(R^{(2),*}, R_t^{(2),*})\|_{C(H^1(\Omega))} \lesssim \|R^{(1),*} - R^{(2),*}\|_{C^1(H^1(\Omega))}.$$

We then have the following analogous result to that of Theorem 3.1.

Theorem 3.2. *Assume that $\Omega \subset \mathbb{R}^d$, $d \in \{2, 3\}$ is a bounded and $C^{2,1}$ -regular domain. Let $c, b > 0$, $\rho > 0$, $\xi \in \mathbb{R}$, $\alpha \in (0, 1)$, and $k \in W^{1,\infty}(\Omega) \cap W^{2,4}(\Omega)$, and let*

$$(p_0, p_1) \in H_{\diamond}^3(\Omega) \times H_{\diamond}^2(\Omega), \quad (R_0, R_1) \in H_{\diamond}^2(\Omega) \times H_{\diamond}^2(\Omega).$$

Furthermore, let h_0 satisfy (3.23) and (3.24). Then there exist pressure data size $\tilde{\delta}_p > 0$, bubble data size $\tilde{\delta}_R$, and time \tilde{T} , such that if

$$\|p_0\|_{H^3(\Omega)} + \|p_1\|_{H^2(\Omega)} \leq \tilde{\delta}_p, \quad \|R_0\|_{H^2(\Omega)} + \|R_1\|_{H^2(\Omega)} \leq \tilde{\delta}_R, \quad \text{and } T \leq \tilde{T},$$

then there is a unique $(p, R) \in \mathfrak{X}_p \times \mathfrak{B}_R$ that solves (3.1) with $\mathcal{A}p = -b\Delta D_t^\alpha p$, where the space \mathfrak{X}_p is defined in (3.20).

Proof. The proof follows analogously to the proof of Theorem 3.1. For $R^* \in \mathfrak{B}_R$, the smallness condition in (3.19) is now replaced by

$$(3.25) \quad \|p_0\|_{H^3(\Omega)} + \|p_1\|_{H^2(\Omega)} + \xi \|((R^*)^3)_{tt}\|_{L^2(H^2(\Omega))} \leq \tilde{\delta}$$

with $\tilde{\delta}$ set by the smallness condition in (3.19). Since

$$\begin{aligned} & \|((R^*)^3)_{tt}\|_{L^2(H^2(\Omega))} \\ & \leq 3\|R^*\|_{L^\infty(H^2(\Omega))}^2 \|R_{tt}^*\|_{L^2(H^2(\Omega))} + 6\|R^*\|_{L^\infty(H^2(\Omega))} \|R_t^*\|_{L^\infty(H^2(\Omega))} \|R_t^*\|_{L^2(H^2(\Omega))} \\ & \leq 3m^2\sqrt{T}M + 6m^3\sqrt{T}, \end{aligned}$$

condition (3.25) is fulfilled for small enough $\tilde{\delta}_p$ and T , similarly to before. The rest of the arguments for proving that \mathfrak{T} is a self-mapping follow in a same manner. When proving strict contractivity of \mathfrak{T} , here we can only exploit the Lipschitz continuity of the pressure field p in the sense of (3.21). Thus, we can use the following bound:

$$\|\bar{\mathcal{R}}\|_{C^2(H^1(\Omega))} \lesssim \|h(R^{(1),*}, R_t^{(1),*}, \mathcal{S}(f(R^{(1),*}))) - h(R^{(2),*}, R_t^{(2),*}, \mathcal{S}(f(R^{(2),*})))\|_{C(H^1(\Omega))}$$

together with (3.21) to prove that \mathfrak{T} is strictly contractive in the norm in $C^2([0, T]; H_0^1(\Omega))$, as opposed to $C^2([0, T]; H_{\diamond}^2(\Omega))$. The rest of the arguments follow analogously to Theorem 3.1 and we thus omit them here. \square

4. NUMERICAL SIMULATION

In this section, we present numerical experiments that illustrate our modeling and analysis considerations. As we want to explore the behavior of microbubbles systematically, we start by examining the dynamics of single microbubbles with a sinusoidal driving pressure. For these simulations, we compare two types of Rayleigh–Plesset equations (RPE), where we vary the amplitude and frequency of the driving pressure to understand how they influence bubble dynamics. Next, we consider a partially decoupled problem of ultrasound–bubble interaction based on the Westervelt–Rayleigh–Plesset system with the zero acoustic source term (that is, with $\xi = 0$). In this context, the pressure input for the Rayleigh–Plesset type equations results from solutions of Westervelt’s equation, allowing us to study the effects of an ultrasound field on bubble behavior. We present results for Westervelt’s equation with strong damping and discuss how fractional attenuation influences the pressure fields and subsequently the behavior of the microbubbles. The program code for all simulations in this section is available as an ancillary file from the arXiv page of this paper.

4.1. Numerical framework for solving Rayleigh–Plesset type equations. For convenience, we restate the Rayleigh–Plesset equations that will be examined numerically in this section. We focus on two concrete equations described in Section 2.4. Our study here centers on the dynamics of single non-coated bubbles using the following Rayleigh–Plesset type equation:

$$(2.39) \quad \rho \left[RR_{tt} + \frac{3}{2} R_t^2 \right] = p_b - 4\mu \frac{R_t}{R} - \frac{2\sigma}{R} + p_{\text{pgn}} \left(\frac{R_0}{R} \right)^{3\kappa} \left(1 - 3\kappa \frac{R_t}{c} \right) - p;$$

and the dynamics of coated bubbles using

$$(2.41) \quad \rho \left[RR_{tt} + \frac{3}{2} R_t^2 \right] = p_b - 4\mu \frac{R_t}{R} - \frac{2\sigma(R)}{R} + p_{\text{pgn}} \left(\frac{R_0}{R} \right)^{3\kappa} \left(1 - 3\kappa \frac{R_t}{c} \right) - 4\kappa_s \frac{R_t}{R^2} - p$$

with

$$\sigma(R) = \chi \left(\frac{R^2}{R_0^2} - 1 \right), \quad p_{\text{pgn}} = \frac{2\sigma_0}{R_0} - p_b, \quad p_b = p_v - p_{\text{stat}}.$$

To ensure accurate and meaningful numerical simulations, we use parameter values typical for ultrasound contrast imaging wherever possible. One of the most widely used ultrasound contrast agents is SonoVue™ (Bracco SpA), see, e.g., [32]. It has a number concentration of $1 \cdot 10^8$ to $5 \cdot 10^8$ microbubbles/mL and the mean diameter of the microbubbles is $2 \mu\text{m}$. Therefore, we choose $R_0 = 2 \mu\text{m}$ as the initial radius for all simulations in the following. Further fixed parameter values are listed in the following table.

χ	shell elasticity	2 N/m
κ	adiabatic exponent	1.4
κ_s	shell viscosity	$2 \cdot 10^{-6} \text{ kg/s}$
μ	shear viscosity	8.9 mPa s
ρ	mass density of the mixture	1000 kg/m^3
σ	surface tension	72.8 mN/m
c	speed of sound	1500 m/s
p_v	vapor pressure	2330 Pa
p_{stat}	static ambient pressure	100 kPa

TABLE 1. Overview of the parameter values used in the simulations.

As we are dealing with second-order ODEs that are nonlinear and singular, the numerical simulations can be instable, highly fluctuating or produce negative values for the bubble radius. These problems especially arise when the radius becomes very small and consequently the rate of change of the radius is extremely large. For these reasons, we use the adaptive time stepping proposed by [22]. The time step in the discrete ODEs is dependent on the size of the bubble radius and chosen according to

$$(4.1) \quad \Delta t(t_i) = [R(t_i)]^\lambda$$

with a time index λ . This means that as the value of λ increases, the time steps become smaller, leading to longer numerical simulations but higher accuracy. By setting $\lambda = 1.75$, we achieve a good balance between computational effort and accuracy, resulting in time steps ranging from 10^{-12}s to 10^{-9}s .

4.2. Single-bubble dynamics. We next delve into the numerical simulations of the Rayleigh–Plesset type equations, specifically focusing on the dynamics of single bubbles under the influence of a sinusoidal driving pressure. This approach allows us to investigate the bubble’s response to periodic pressure variations, observing different forms of bubble oscillations and stability.

We consider a sinusoidal driving pressure function of the form

$$p(t) = A \sin(2\pi ft)$$

where, in this section, f is the driving frequency and A is the amplitude. We present selected settings for various values of A and f in the following. The simulations are performed in Python using a fourth order Runge-Kutta scheme with the adaptive time stepping given by (4.1). First, we aim to provide an intuitive understanding of the solutions to the Rayleigh–Plesset type equations. We begin by examining the Rayleigh–Plesset type equation for coated bubbles, as it offers a more realistic model. Figure 2 shows the Radius-time curves $R(t)$ of this equation given in (2.41), with varying amplitudes $A = 1, 5, 10$ MPa and driving frequencies $f = 0.2, 0.5$ MHz.

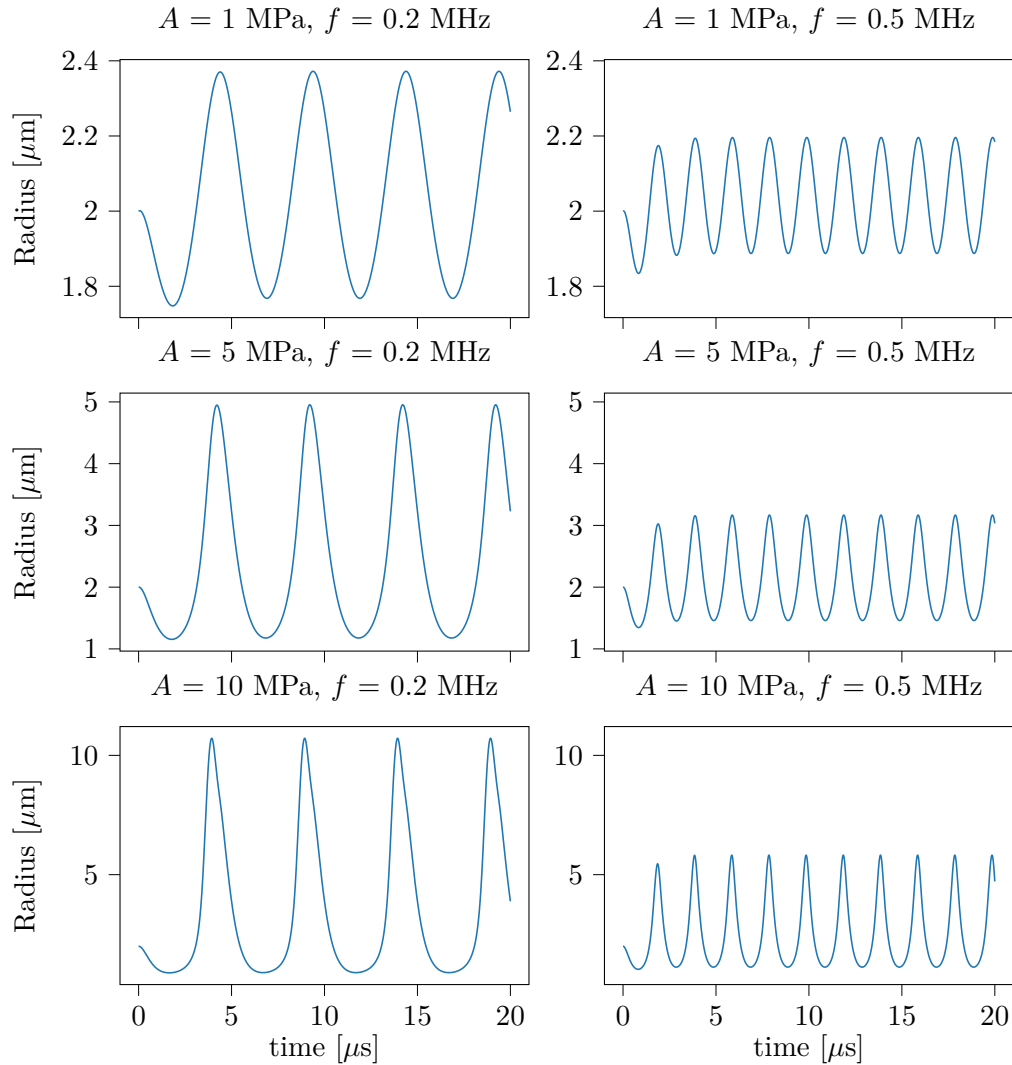


FIGURE 2. Sensitivity of coated bubbles to driving amplitude and frequency: Radius-time $R(t)$ curves for different amplitudes $A = 1, 5, 10$ MPa and driving frequencies $f = 0.2, 0.5$ MHz of the RPE for coated bubbles given in eq. (2.41).

The results in Figure 2 clearly illustrate the influence of the driving pressure on the bubbles' radii. At low forcing levels, the microbubbles exhibit almost sinusoidal oscillations with relatively small amplitude. As the forcing pressure increases, the effects of nonlinearity become significantly more pronounced. Specifically, for a fixed frequency, we observe that the curve representing the radius steepens, and the amplitude of the radius increases as the pressure amplitude rises. Conversely, when comparing different frequencies but maintaining the same pressure amplitude, lower frequencies reveal more nonlinear effects, with the amplitude of the radius being higher. This indicates that both the magnitude of the driving pressure and the frequency play crucial roles in dictating the bubble's dynamic behavior.

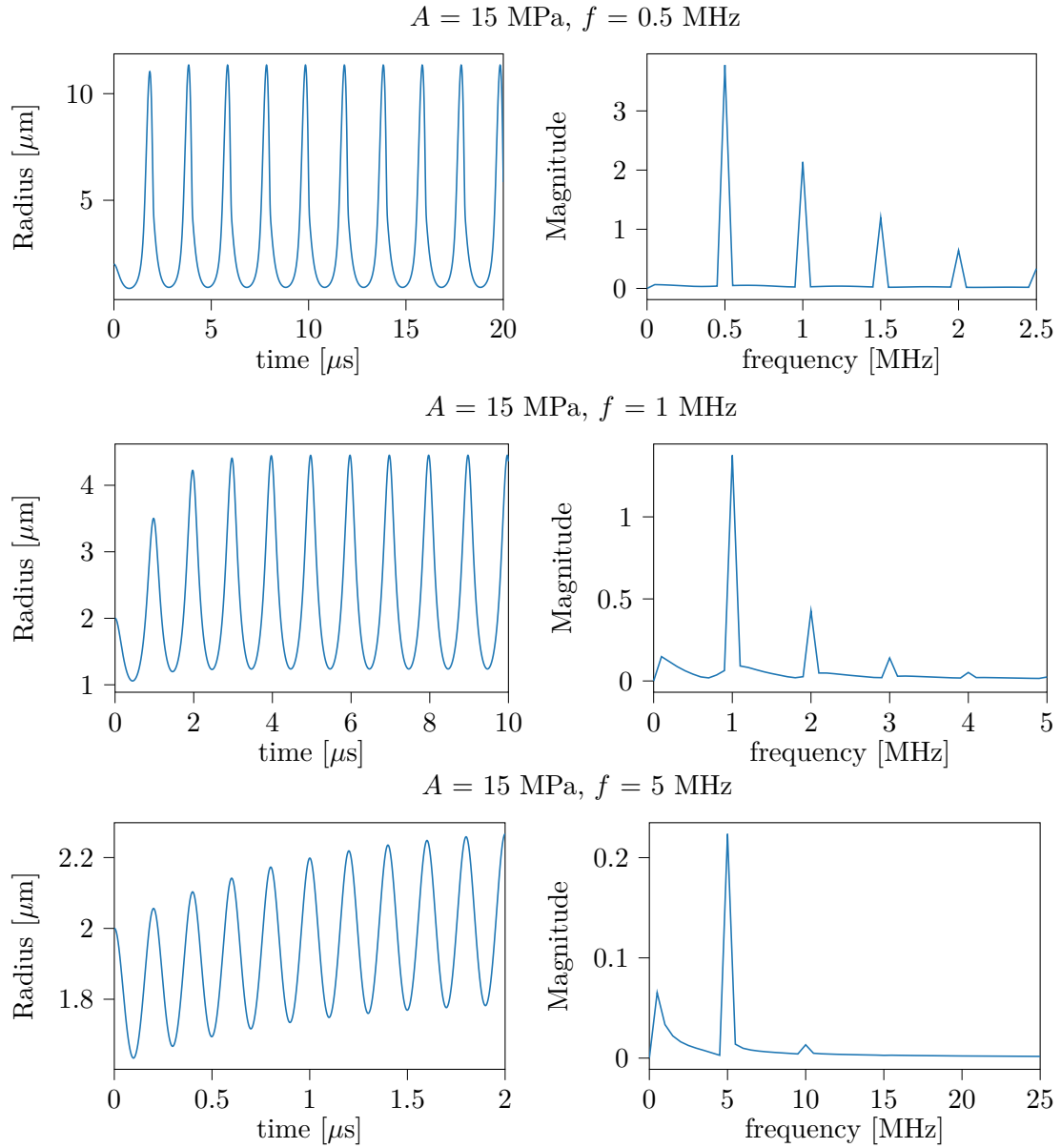


FIGURE 3. Behavior for high frequencies: Radius-time $R(t)$ curves and the corresponding FFT-spectra for the amplitude $A = 15$ MPa and different driving frequencies $f = 0.5, 1, 5$ MHz of the RPE for coated bubbles given in eq. (2.41).

The typical frequency range used in diagnostic ultrasound imaging is 1 to 10 MHz. For the amplitude of the driving pressure values between 10 and 15 MPa are realistic. Figure 3 shows Radius-time $R(t)$ curves for coated bubbles and the corresponding fast Fourier transform (FFT) - spectra for the amplitude $A = 15$ MPa and different driving frequencies $f = 0.5, 1, 5$ MHz. To facilitate a thorough comparison, we examine 10 cycles of the curves in time domain and the corresponding frequency spectra. The results indicate that nonlinear effects decrease as the frequency increases.

For the smallest frequency of 0.5 MHz the radius curve is very steep and the bubble reaches approximately six times its initial size. In frequency domain the harmonics at multiples of the fundamental frequency are clearly visible and far more intense at a driving frequency of 0.5 MHz compared to higher frequencies of 1 and 5 MHz. This is probably at least partially due to stronger attenuation at higher frequencies, as also visible in the reduced amplitudes (around 10 μm at 0.5 MHz and only around 2 μm at 5 MHz).

Next, we want to compare the radius plots resulting from the Rayleigh–Plesset type equation for coated bubbles, given by equation (2.41), with those from equation (2.39) for non-coated bubbles, where the shell terms are neglected.

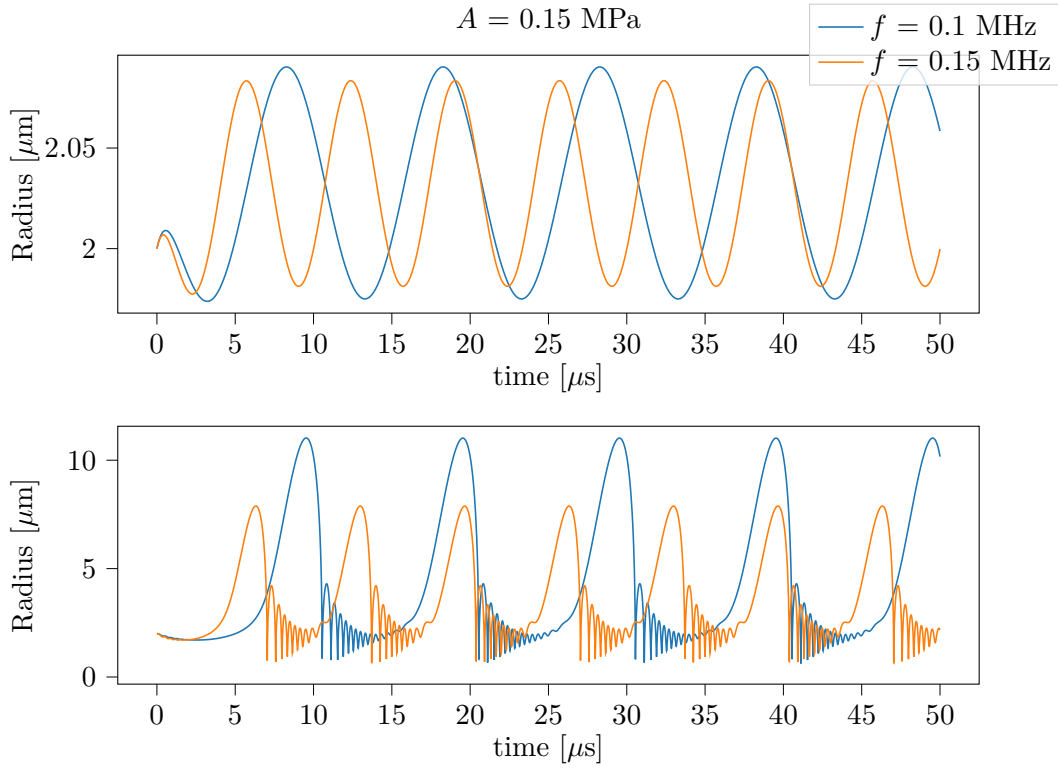


FIGURE 4. Comparison of ODE models: Radius-time $R(t)$ curves for the amplitude $A = 0.15$ MPa and different driving frequencies $f = 0.1$ (blue), 0.15 (orange) MHz of the RPE for coated bubbles given in eq. (2.41) (top) and non-coated bubbles given in eq. (2.39) (bottom).

The presence of a shell adds stability to the bubbles by reducing nonlinearities and keeping the radius amplitude smaller. For an amplitude of $A = 0.15$ MPa and driving frequencies $f = 0.1, 0.15$ MHz, the first plot at the top in Figure 4 shows the numerical solutions $R = R(t)$ of the ODE (2.41) and the second one of equation (2.39). The simulations that take the shell

terms into account show a sinusoidal behavior with an amplitude close to the initial radius. The non-coated bubble expands approximately four to six times its initial radius, drops extremely quickly and afterbounces roughly with its eigenfrequency. This clearly illustrates that the shell protects the bubbles and dampens the fluctuations in the bubble radius.

To complete our study of single-microbubble dynamics, we also consider the Rayleigh–Plesset type equation for non-coated bubbles on its own.

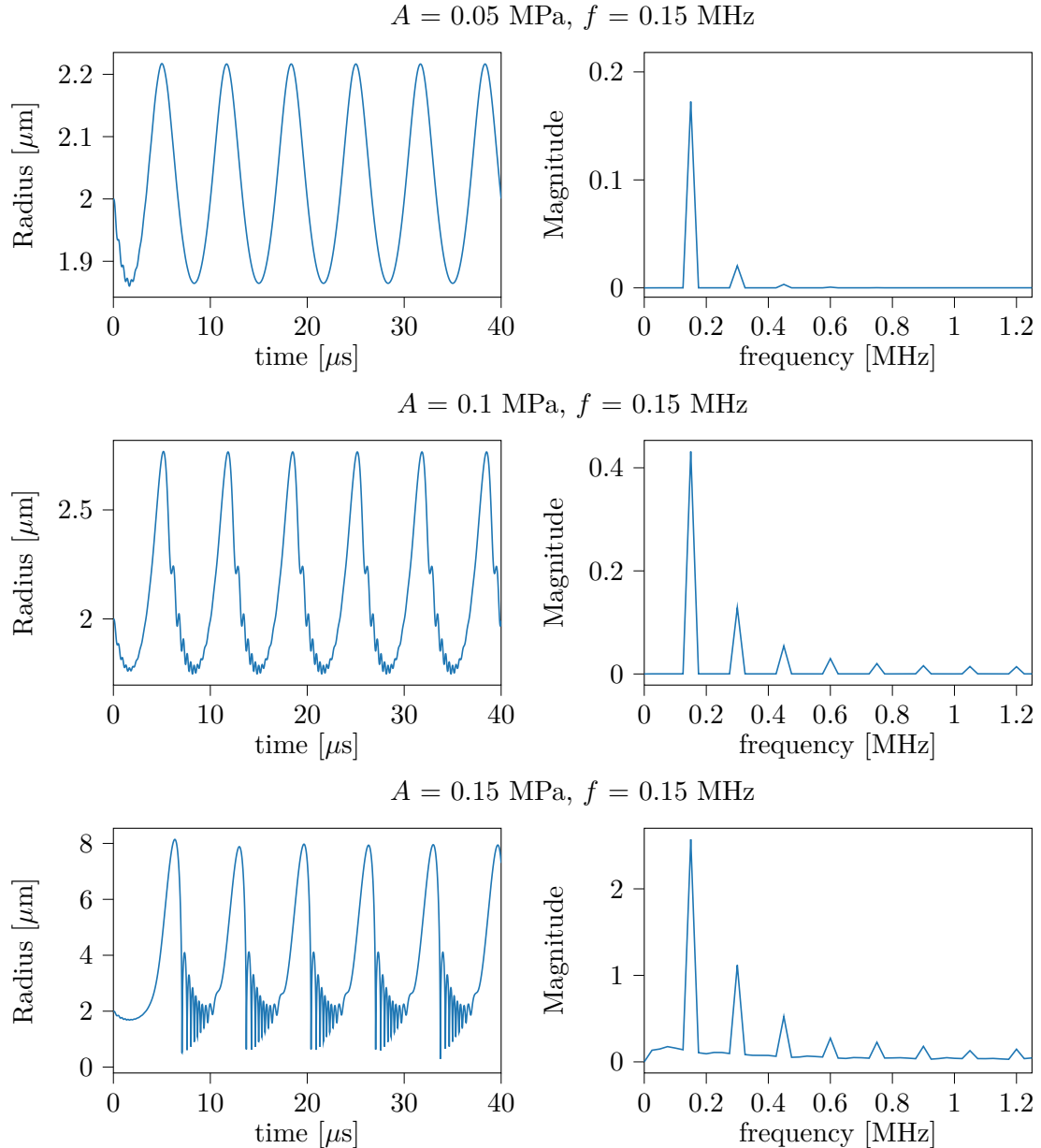


FIGURE 5. Behavior of non-coated bubbles: Radius-time $R(t)$ curves and the corresponding FFT-spectra for the driving frequency $f = 0.15 \text{ MHz}$ and different amplitudes $A = 0.05, 0.1, 0.15 \text{ MPa}$ of the RPE for non-coated bubbles given in eq. (2.39).

Given the inherent instability of this model, high amplitudes and frequencies – typical in ultrasound contrast imaging – can cause numerical instabilities. When these parameters are increased to more realistic levels, as shown in Figure 3 for coated bubbles, the simulation of equation (2.39) becomes unstable, resulting in negative radius values. Therefore, we consider driving amplitudes of $A = 0.05, 0.01, 0.15$ MPa with a fixed frequency of $f = 0.15$ MHz. The resulting Radius-time curves $R(t)$ are presented in Figure 5, illustrating different regimes of bubble oscillation behavior: from sinusoidal patterns to large bubble growth followed by a steep drop and rebounds. As the amplitude increases, the time-domain curves exhibit small oscillations, which can be observed in the frequency domain as higher harmonics rise, indicating stronger nonlinear effects.

Note that in Figure 3, we have kept the driving amplitude constant while varying the frequencies, whereas in Figure 5, we have varied the amplitudes with a fixed frequency. This comparison reveals that nonlinear effects in microbubble dynamics intensify as the driving frequency decreases and the driving amplitude increases.

4.3. Ultrasound-microbubble interaction. In the course of this section, we present numerical results for the Westervelt–Rayleigh–Plesset model. To simplify the computational complexity somewhat, we set the right-hand source term in the Westervelt equation to zero. To reflect a more realistic computational setting, we set up a domain that allows focusing of sound waves. Furthermore, we employ Neumann boundary conditions in the simulations and zero pressure data. All simulations of Westervelt’s equation are performed in Python using FEniCSx v0.7.2; see, e.g., [2]. The simulation is based on continuous linear finite elements for spatial discretization and a predictor-corrector Newmark scheme for time integration, following the algorithm in [11, Ch. 5]. The integration parameters in the Newmark scheme are set to $\gamma = 0.7$ and $\beta = 0.4$ and the time step is taken to be $3 \cdot 10^{-6}$ s. Note that this time step size differs by six orders of magnitude compared to the time stepping used for the ODEs. The significant difference in time step sizes introduces challenges, particularly in ensuring stability and accuracy across different time scales. To achieve focusing we construct a rectangular domain with one curved side, where the waves are excited such that they nicely focus at the center of the domain. This setup was created using Gmsh; see, e.g., [9].

4.3.1. The Westervelt–Rayleigh–Plesset model with strong acoustic damping. We simulate the following system:

$$(4.2) \quad \begin{cases} ((1 + 2k(x)p)p_t)_t - c^2 \Delta p - b \Delta p_t = 0 \\ \rho \left[RR_{tt} + \frac{3}{2} R_t^2 \right] = p_b - 4\mu \frac{R_t}{R} - \frac{2\sigma(R)}{R} + p_{\text{pgn}} \left(\frac{R_0}{R} \right)^{3\kappa} \left(1 - 3\kappa \frac{R_t}{c} \right) - 4\kappa_s \frac{R_t}{R^2} - p \end{cases}$$

and begin by presenting pressure waves generated from the acoustic equation in (4.2) with strong acoustic damping using Neumann boundary conditions and zero initial data, within a focused domain. The Neumann conditions are given by $\frac{\partial p}{\partial n} = A_p \sin(2\pi f_p t)$ on the curved part of the boundary of the computational domain, and set to zero elsewhere. The amplitude of the acoustic boundary excitation is taken to be $A_p = 0.1$ MPa/m and the frequency $f_p = 15$ kHz.

Figure 6 presents the pressure wave forms generated from Westervelt’s equation within a two-dimensional spatial domain. The focal region, the area with the highest peak of the pressure waves, is clearly visible and shows the point of maximum pressure intensity. Additionally, the figure highlights nonlinear effects: the positive peak pressure surpasses the negative values, indicating an asymmetry in the pressure distribution and the side profile of the waveform shows noticeable steepening.

Time: 0.000660

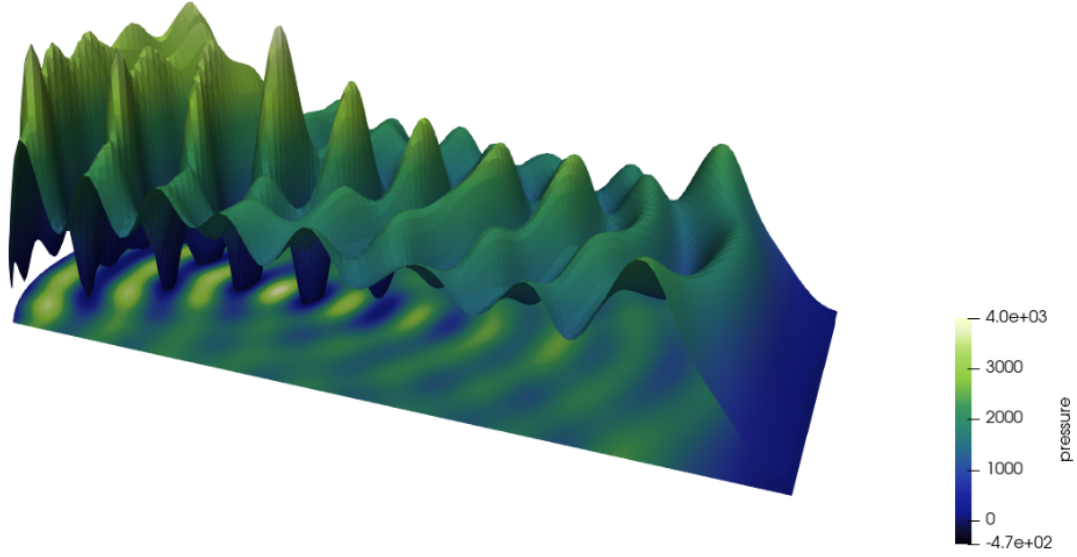


FIGURE 6. Nonlinear acoustic waves: Propagation and self focusing of pressure waves. The plot is obtained using Westervelt's equation with strong damping in (4.2) on a 2D spatial domain.

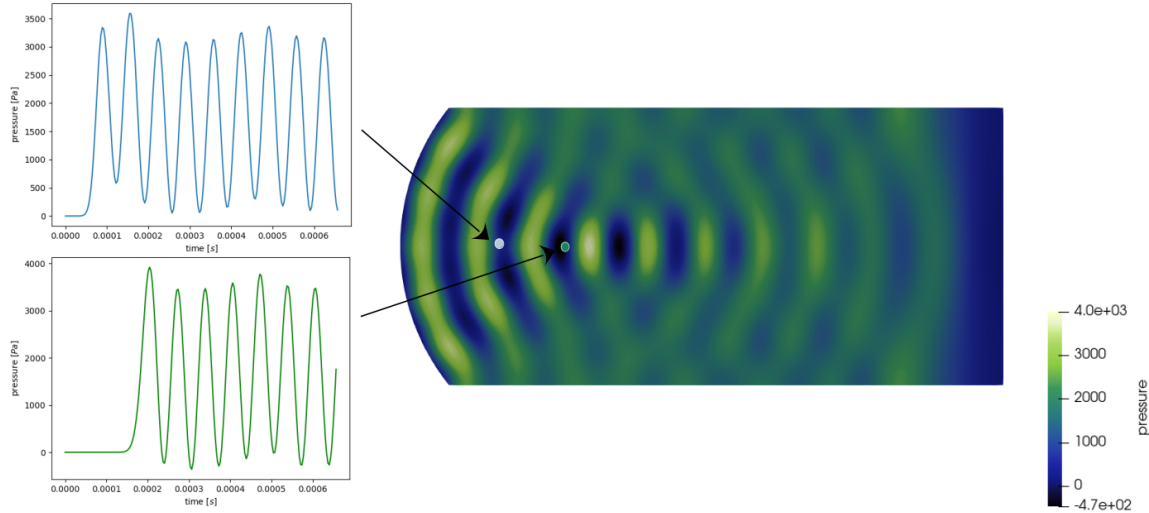


FIGURE 7. Westervelt input for RPE: Acoustic pressure waves over time at two different spatial points obtained using Westervelt's equation. The acoustic field serves input for the Rayleigh–Plesset type equations; see (4.2).

Next, we select two pressure-time curves obtained from Westervelt's equation with strong acoustic damping along the central axis to serve as inputs for the Rayleigh–Plesset type equations. An overview of these curves is provided in Figure 7. The first curve, depicted in blue, is representative of the pressure close to the excitation source. In contrast, the second curve, shown in green, corresponds to the focal region where the pressure is more intense. As a result,

the green curve demonstrates more prominent nonlinear effects compared to the blue one. We chose to examine these two curves for the problem stated in (4.2) in order to understand how different regions within the acoustic field influence microbubble behavior. The results of this analysis are illustrated in Figure 8. It is evident that the amplitude of the green radius-time curve is significantly higher compared to the blue curve. This increase in amplitude is a direct result of the greater intensity of the pressure input represented by the green curve. The corresponding frequency spectra further highlight this effect, revealing that while higher harmonics are not prominently visible, subharmonics seem to appear. When comparing these findings to the results presented in Section 4.2, where a sinusoidal driving pressure was used, it becomes apparent that the radius-time curves shown in Figure 8 exhibit greater symmetry with respect to the x -axis and demonstrate expanding bubble behavior. As expected, a sinusoidal driving pressure leads to enhanced stability and generates periodic radius-time curves. This comparison underscores the differences in microbubble dynamics influenced by varying pressure inputs.

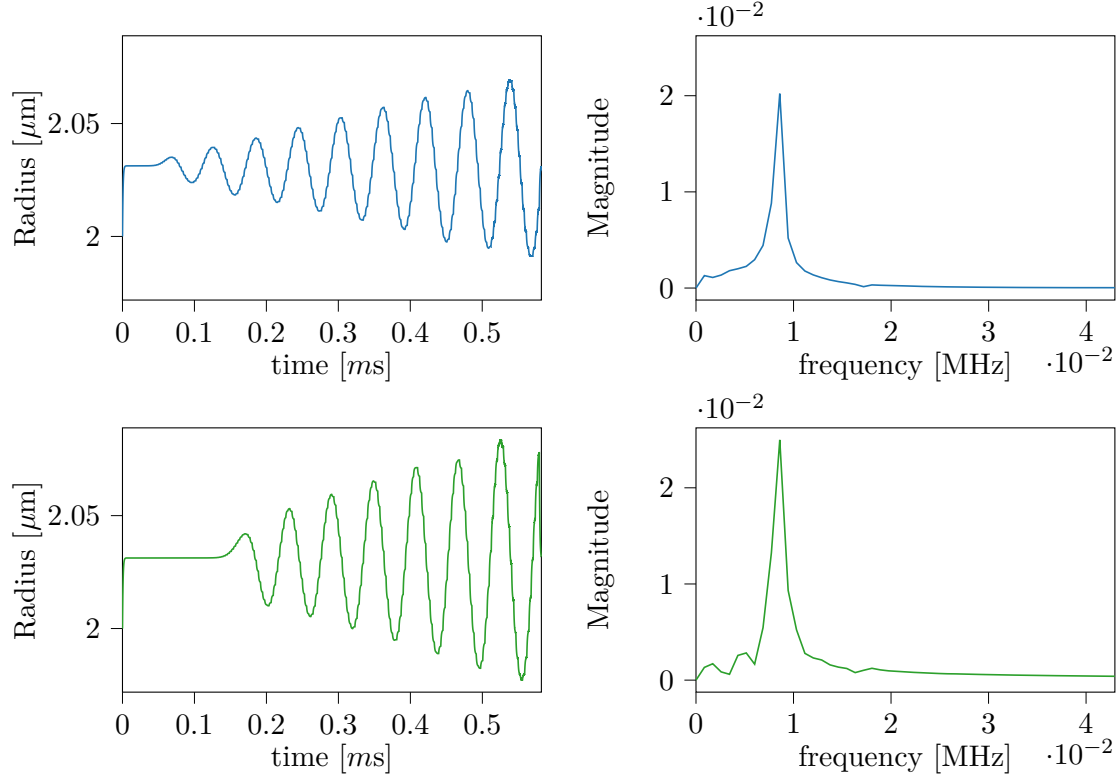


FIGURE 8. Coated bubbles with Westervelt input: Radius-time $R(t)$ curves of RPE for coated bubbles given in (2.41) with Westervelt type pressure input p at two different positions in the domain; see also Figure 7.

To complete our investigation within this framework, we conclude this section by examining the problem involving Westervelt's equation in conjunction with the Rayleigh–Plesset type equation, which excludes shell terms as specified in (2.39).

The results presented in Figure 9 reveal that this ODE exhibits greater instability and stronger nonlinear effects. In particular, the frequency domain analysis shows an increase in higher harmonics, a trend that becomes more pronounced with higher pressure input intensities. Additionally, the gradients of the radius-time curves are steeper, the curves display reduced symmetry, and the amplitudes are greater compared to those shown in Figure 8.

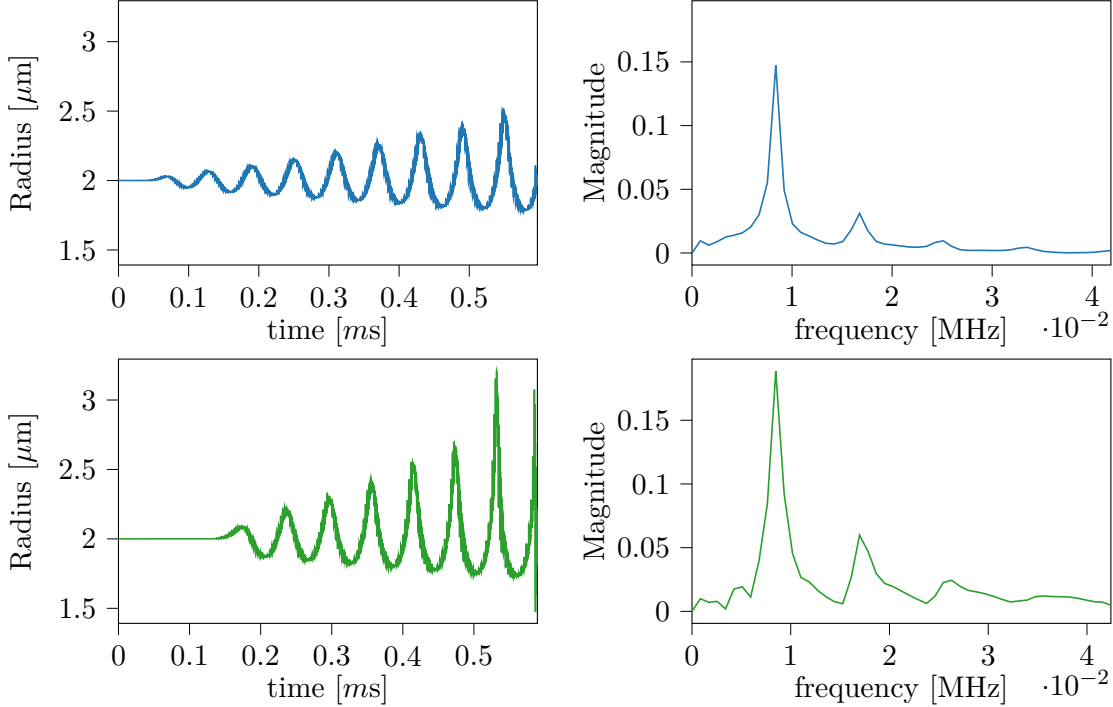


FIGURE 9. Non-coated bubbles with Westervelt input: Radius-time $R(t)$ curves of RPE for non-coated bubbles given in equation (2.39) with Westervelt type pressure input p at two different positions in the domain; see also Figure 7.

4.3.2. *Fractional acoustic attenuation.* We also consider the Westervelt–Rayleigh–Plesset model with fractional attenuation given by

$$\begin{cases} ((1 + 2k(x)p)p_t)_t - c^2 \Delta p - b\tau^{\alpha-1} D_t^\alpha \Delta p = 0 \\ \rho \left[RR_{tt} + \frac{3}{2} R_t^2 \right] = p_b - 4\mu \frac{R_t}{R} - \frac{2\sigma(R)}{R} + p_{\text{pgn}} \left(\frac{R_0}{R} \right)^{3\kappa} \left(1 - 3\kappa \frac{R_t}{c} \right) - 4\kappa_s \frac{R_t}{R^2} - p. \end{cases}$$

The Caputo–Djrbashian fractional derivative is discretized using an L1-type scheme following the algorithm in [17]. We set the relaxation time to $\tau = 10^{-12}$ s and the order of the fractional derivative to $\alpha = 0.5$. Under the same setting as before in terms of data and computational domain, we have carried out simulations similar to those described in Section 4.3.1 and observed effects that were very comparable. Since these results do not reveal significant qualitative differences in microbubble dynamics, we do not present them here. Instead, we briefly discuss the differences observed in the Westervelt equation with strong damping and fractional attenuation.

Westervelt's equation with strong damping is expected to produce a pressure wave with a smaller amplitude and less pronounced nonlinear effects. In Figure 10, the red curve, which corresponds to fractional attenuation, is steeper and more asymmetric, indicating greater nonlinear contributions. However, the amplitude of the red curve is lower than of the green one. This occurs because the additional factor $\tau^{\alpha-1}$ in front of the damping term increases the damping effect, leading to more significant attenuation. This slight difference in the pressure-time curve translates into the radius-time curves, which essentially leads to a modest decrease in amplitude.

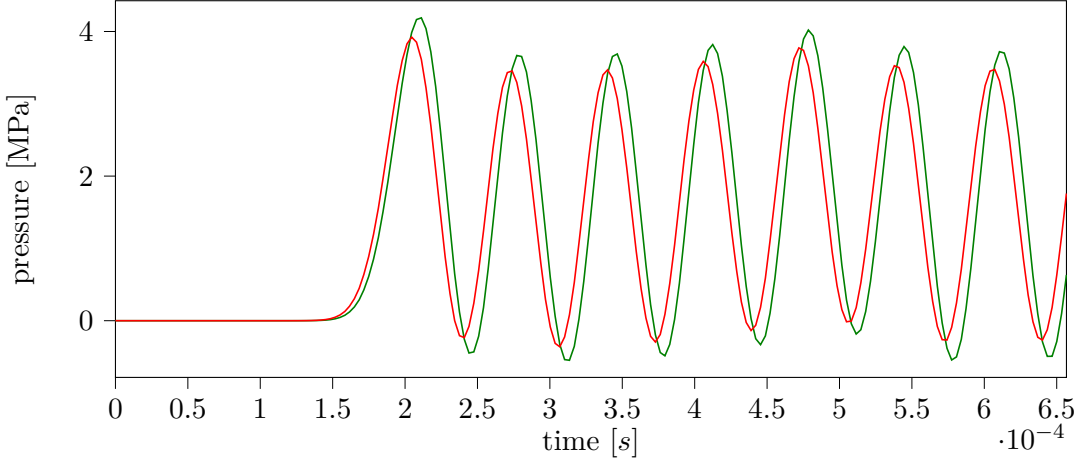


FIGURE 10. Pressure-time curves of Westervelt's equation with strong damping (green) and fractional attenuation with $\alpha = 0.5$ and $\tau = 10^{-12}\text{s}$ (red) at a spatial point.

5. CONCLUSION AND OUTLOOK

In this work, we have explored the mathematical modeling and analysis of ultrasound contrast imaging, with a focus on the nonlinear interactions between microbubbles and sound waves. By deriving and analyzing coupled wave-ODE systems, including the Westervelt–Rayleigh–Plesset model, we have gained novel theoretical and numerical insights into the dynamics of microbubble oscillations under varying conditions of acoustic pressure. Our findings contribute to the understanding and optimization of ultrasound-based technologies, with implications for developing both imaging and therapeutic applications.

Outlook. Future research could focus on several key areas to advance the current understanding and use of ultrasound contrast imaging. Adapting the mathematical analysis to the setting of Neumann or absorbing acoustic boundary conditions is important for modeling more realistic scenarios, where one should avoid non-physical reflections of sound waves. Furthermore, extending the analysis to address the refined wave-ODE models derived in Section 2, such as (2.23), would provide deeper insights into the complex interactions between acoustic waves and microbubble dynamics.

From a numerical perspective, addressing the fully coupled problem (3.1) with $\xi \neq 0$, where both wave propagation and microbubble dynamics are solved simultaneously, would be a significant step forward in capturing the complete range of physical behaviors. This setting introduces additional computational complexity, particularly due to the need for much finer time steps in discretizing the ODE compared to the wave equation, which already need to be relatively small in the nonlinear acoustic setting. Techniques such as multirate time stepping and operator splitting methods could be explored to manage these differing time scales.

Finally, the inverse problem of determining the spatially varying acoustic nonlinearity coefficient $k = k(x)$ in the ultrasound-microbubble system from given data presents a compelling area for investigation, both theoretically and computationally. Solving it could pave the way to more precise imaging techniques with enhanced diagnostic capabilities.

Acknowledgments. We are very grateful to Barbara Kaltenbacher for her valuable comments throughout the project.

This research was funded in part by the Austrian Science Fund (FWF) [10.55776/DOC78].

For open access purposes, the authors have applied a CC BY public copyright license to any author-accepted manuscript version arising from this submission.

A. LIPSCHITZ CONTINUITY RESULTS

We present here the derivation of estimates in (3.4) and (3.21) for the pressure field.

Lemma A.1. *Under the assumptions of Proposition 3.1, let $p^{(1)}$ and $p^{(2)}$ be the solutions of (3.1) with the right-hand sides $f_1 \in L^2(0, T; L^2(\Omega))$ and $f_2 \in L^2(0, T; L^2(\Omega))$, respectively. Then*

$$\|p^{(1)} - p^{(2)}\|_{C(H^2(\Omega))} \lesssim \|f_1 - f_2\|_{L^2(L^2(\Omega))}.$$

Proof. Thanks to Proposition 3.1, $p^{(1)}, p^{(2)} \in X_p$, and

$$(A.1) \quad \|p^{(1)}\|_{X_p}, \|p^{(2)}\|_{X_p} \leq C$$

for some $C > 0$. The difference $\bar{p} = p^{(1)} - p^{(2)}$ solves

$$(1 + 2k(x)p^{(1)})\bar{p}_{tt} - c^2\Delta\bar{p} - b\Delta\bar{p}_t = f_1 - f_2 - 2k(x)(\bar{p}\bar{p}_{tt}^{(2)} + \bar{p}_t(p^{(1)} + p^{(2)})).$$

with homogeneous boundary and initial data. The claim follows by testing this difference equation with $\bar{p}_{tt} - \Delta\bar{p} \in L^2(0, T; L^2(\Omega))$, integrating over Ω and $(0, t)$, and performing integration by parts in time and space, analogously to the arguments in the proof of contractivity in [16, Proposition 1]. In this way, we obtain

$$(A.2) \quad \begin{aligned} & \int_0^t \|\sqrt{1 + 2kp^{(1)}}\bar{p}_{tt}\|_{L^2(\Omega)}^2 ds + c^2 \int_0^t \|\Delta\bar{p}\|_{L^2(\Omega)}^2 ds + \frac{b}{2} \|\Delta\bar{p}(t)\|_{L^2(\Omega)}^2 + \frac{b}{2} \|\nabla\bar{p}_t\|_{L^2(\Omega)}^2 \\ & \leq \int_0^t \int_{\Omega} ((1 + 2kp^{(1)})\bar{p}_{tt})\Delta\bar{p} dx ds + c^2 \int_0^t \int_{\Omega} \Delta\bar{p}\bar{p}_{tt} dx ds \\ & \quad + \int_0^t \int_{\Omega} (f_1 - f_2)(\bar{p}_{tt} - \Delta\bar{p}) dx ds \\ & \quad - 2 \int_0^t \int_{\Omega} k(x)(\bar{p}\bar{p}_{tt}^{(2)} + \bar{p}_t(p^{(1)} + p^{(2)}))(\bar{p}_{tt} - \Delta\bar{p}) dx ds. \end{aligned}$$

The right-hand side terms in (A.4) can be estimated using Hölder's and Young's inequalities in a straightforward manner. Indeed, on account of (A.1), we have

$$\begin{aligned} \int_0^t \int_{\Omega} ((1 + 2kp^{(1)})\bar{p}_{tt})\Delta\bar{p} dx ds & \leq \|1 + 2kp^{(1)}\|_{L^\infty(L^\infty(\Omega))} \|\bar{p}_{tt}\|_{L^2(0,t;L^2(\Omega))} \|\Delta\bar{p}\|_{L^2(0,t;L^2(\Omega))} \\ & \lesssim \varepsilon \|\bar{p}_{tt}\|_{L^2(0,t;L^2(\Omega))}^2 + \|\Delta\bar{p}\|_{L^2(0,t;L^2(\Omega))}^2 \end{aligned}$$

for any $\varepsilon > 0$. Furthermore,

$$\begin{aligned} \int_0^t \int_{\Omega} (f_1 - f_2)(\bar{p}_{tt} - \Delta\bar{p}) dx ds & \leq \frac{1}{2\varepsilon} \|f_1 - f_2\|_{L^2(0,t;L^2(\Omega))}^2 + \varepsilon \|\bar{p}_{tt}\|_{L^2(0,t;L^2(\Omega))}^2 \\ & \quad + \varepsilon \|\Delta\bar{p}\|_{L^2(0,t;L^2(\Omega))}^2, \end{aligned}$$

and the other terms can be treated analogously. By choosing a sufficiently small $\varepsilon > 0$ and employing these estimates in (A.2), the \bar{p}_{tt} terms on the right-hand sides can be absorbed by the left-hand side, whereas the $\Delta\bar{p}$ terms can be subsequently handled using Grönwall's inequality. In this manner, we obtain the claimed estimate. \square

Lemma A.2. *Under the assumptions of Proposition 3.2, let $p^{(1)}$ and $p^{(2)}$ be the solutions of (3.1) with the right-hand sides $f_1 \in L^2(0, T; H_{\diamond}^2(\Omega))$ and $f_2 \in L^2(0, T; H_{\diamond}^2(\Omega))$, respectively. Then*

$$\|p^{(1)} - p^{(2)}\|_{C^1(L^2(\Omega))} + \|p^{(1)} - p^{(2)}\|_{C(H^1(\Omega))} \lesssim \|f_1 - f_2\|_{L^2(L^2(\Omega))}.$$

Proof. According to Proposition 3.2, $p^{(1)}, p^{(2)} \in \mathfrak{X}_p$, and

$$(A.3) \quad \|p^{(1)}\|_{\mathfrak{X}_p}, \|p^{(2)}\|_{\mathfrak{X}_p} \leq C$$

for some $C > 0$. The difference $\bar{p} = p^{(1)} - p^{(2)}$ solves

$$(1 + 2k(x)p^{(1)})\bar{p}_{tt} - c^2\Delta\bar{p} - b\Delta D_t^\alpha\bar{p} = f_1 - f_2 - 2k(x)(\bar{p}p_{tt}^{(2)} + \bar{p}_t(p^{(1)} + p^{(2)})).$$

with homogeneous boundary and initial data. The statement follows by testing this difference equation with \bar{p}_t , integrating over Ω and $(0, t)$, and performing integration by parts in time and space, similarly to the arguments in the proof of contractivity in [13, Theorem 3.1]. Indeed, in this manner, we obtain

$$(A.4) \quad \begin{aligned} & \frac{1}{2}\|\sqrt{1 + 2kp^{(1)}}\bar{p}_t(t)\|_{L^2(\Omega)}^2 + \frac{c^2}{2}\|\nabla\bar{p}(t)\|_{L^2(\Omega)}^2 \\ & \leq \int_0^t \int_\Omega k(x)p_t^{(1)}\bar{p}_t^2 \, dx \, ds + \int_0^t \int_\Omega (f_1 - f_2)\bar{p}_t \, dx \, ds \\ & \quad - 2 \int_0^t \int_\Omega k(x)(\bar{p}p_{tt}^{(2)} + \bar{p}_t(p^{(1)} + p^{(2)}))\bar{p}_t \, dx \, ds. \end{aligned}$$

Above we have relied on

$$-b \int_0^t \int_\Omega \Delta D_t^\alpha \bar{p} \bar{p}_t \, dx \, ds = b \int_0^t \int_\Omega \nabla D_t^\alpha \bar{p} \cdot \nabla \bar{p}_t \, dx \, ds \geq 0,$$

where the non-negativity follows by the properties of the Abel kernel $\mathfrak{K}(t) = \frac{1}{\Gamma(1-\alpha)}t^{-\alpha}$; see, e.g., [13, Lemma 5.1]. On account of (A.3), the right-hand side terms in (A.4) can be estimated using Hölder's inequality in a straightforward manner, after which an application of Grönwall's inequality yields the desired bound. \square

Finally, we prove here that assumptions (3.8) and (3.9) hold for the right-hand side h_0 in the Rayleigh–Plesset equation given by

$$(2.42) \quad h_0(R, R_t) = p_b - \frac{4\mu}{R}R_t - \frac{2\sigma(R)}{R} + p_{\text{pgn}} \left(\frac{R_0}{R} \right)^{3\kappa} \left(1 - 3\kappa_0 \frac{R_t}{c} \right) - 4\kappa_s \frac{R_t}{R^2},$$

where σ is a constant or given by (2.40) and $\kappa_s, \kappa_0 \in \mathbb{R}$, provided $R \in \mathcal{B}_R$. The estimates given in (3.23) and (3.24) for $R \in \mathfrak{B}_R$ in the time-fractional setting follow analogously.

Lemma A.3. *Under the assumptions of Theorem 3.1, let $R^{(1)*}, R^{(2)*} \in \mathcal{B}_R$, where \mathcal{B}_R is defined in (3.7). Let h_0 be given by (2.42) with $p_b, p_{\text{pgn}} \in C([0, T]; L^\infty(\Omega))$, $\kappa \geq 1$, $\kappa_0, \kappa_s, \mu \in \mathbb{R}$, and $R_0 > 0$. Assume σ is either a real constant or given by (2.40) with $\chi \in \mathbb{R}$. Then h_0 satisfies (3.8) and (3.9).*

Proof. We provide the proof of (3.9). We can rewrite the difference of h_0 terms as follows:

$$\begin{aligned}
& h_0(R^{(1),*}, R_t^{(1),*}) - h_0(R^{(2),*}, R_t^{(2),*}) \\
&= -\frac{1}{R^{(1),*}R^{(2),*}}p_b(R^{(1),*} - R^{(2),*}) - 4\mu\frac{\bar{\mathcal{R}}_t^* R^{(2),*} + R_t^{(2),*} \bar{\mathcal{R}}^*}{R^{(1),*}R^{(2),*}} \\
&\quad - 2\frac{\sigma(R^{(1),*})\bar{\mathcal{R}}^* + (\sigma(R^{(1),*}) - \sigma(R^{(2),*}))R^{(2),*}}{R^{(1),*}R^{(2),*}} \\
(A.5) \quad &+ p_{pgn}\left(\frac{R_0}{R^{(1),*}}\right)^{3\kappa}\left(1 - 3\kappa_0\frac{R^{(1),*}}{c}\right) - p_{pgn}\left(\frac{R_0}{R^{(2),*}}\right)^{3\kappa}\left(1 - 3\kappa_0\frac{R^{(2),*}}{c}\right) \\
&\quad - 4\kappa_s\frac{1}{(R^{(1),*})^2}\bar{\mathcal{R}}^* - 4\kappa_s R_t^{(2),*}\frac{\bar{\mathcal{R}}^*}{(R^{(1),*}R^{(2),*})^2}.
\end{aligned}$$

Note that since $R^{(1),*} \in \mathcal{B}_R$, we have

$$\|\sigma(R^{(1),*})\|_{C(L^\infty(\Omega))} \lesssim 1 + \|R^{(1),*}\|_{C(L^\infty(\Omega))}^2 \lesssim 1 + m^2.$$

Using

$$\left(\frac{1}{R^{(1),*}}\right)^{3\kappa} - \left(\frac{1}{R^{(2),*}}\right)^{3\kappa} = \left(\frac{1}{R^{(1),*}R^{(2),*}}\right)^{3\kappa} \bar{\mathcal{R}}^\kappa \left((R^{(1),*})^2 + R^{(1),*}R^{(2),*} + (R^{(2),*})^2\right)^\kappa$$

as well as

$$\|\sigma(R^{(1),*}) - \sigma(R^{(2),*})\|_{C(L^\infty(\Omega))} \leq \frac{|\chi|}{R_0^2} \|\bar{\mathcal{R}}\|_{C(L^\infty(\Omega))} (\|R^{(1),*}\|_{C(L^\infty(\Omega))} + \|R^{(2),*}\|_{C(L^\infty(\Omega))})$$

and the fact that the radii are uniformly bounded:

$$0 < \underline{R} \leq R^{(1),*}, R^{(2),*} \leq \bar{R}, \quad \|R^{(1),*}\|_{C^1(L^\infty(\Omega))} + \|R^{(2),*}\|_{C^1(L^\infty(\Omega))} \lesssim m,$$

from (A.5) we obtain

$$\begin{aligned}
& \|h_0(R^{(1),*}, R_t^{(1),*}) - h_0(R^{(2),*}, R_t^{(2),*})\|_{C(L^\infty(\Omega))} \\
& \lesssim \|R^{(1),*} - R^{(2),*}\|_{C(L^\infty(\Omega))} + \|R_t^{(1),*} - R_t^{(2),*}\|_{C(L^\infty(\Omega))},
\end{aligned}$$

as claimed. \square

REFERENCES

- [1] K. BAKER, L. BANJAI, AND M. PTASHNYK, *Numerical analysis of a time-stepping method for the Westervelt equation with time-fractional damping*, Mathematics of Computation, (2024).
- [2] I. A. BARATTA, J. P. DEAN, J. S. DOKKEN, M. HABERA, J. S. HALE, C. N. RICHARDSON, M. E. ROGNES, M. W. SCROGGS, N. SIME, AND G. N. WELLS, *DOLFINx: The next generation FEniCS problem solving environment*, Dec. 2023.
- [3] Z. BIRO AND J. VELAZQUEZ, *Analysis of a free boundary problem arising in bubble dynamics*, SIAM Journal on Mathematical Analysis, 32 (2000), pp. 142–171.
- [4] D. T. BLACKSTOCK, *Approximate Equations Governing Finite-amplitude Sound in Thermoviscous Fluids*, Defense Technical Information Center, 1963.
- [5] C. E. BRENNEN, *Cavitation and Bubble Dynamics*, Cambridge University Press, 2013.
- [6] D. G. CRIGHTON, *Nonlinear Acoustic of Bubbly Liquids*, Springer Vienna, Vienna, 1991, pp. 45–68.
- [7] A. DEKKERS AND A. ROZANOVA-PIERRAT, *Cauchy problem for the Kuznetsov equation*, Discrete & Continuous Dynamical Systems - A, 39 (2019), pp. 277–307.

- [8] A. A. DOINIKOV AND A. BOUAKAZ, *Review of shell models for contrast agent microbubbles*, IEEE transactions on ultrasonics, ferroelectrics, and frequency control, 58 (2011), pp. 981–993.
- [9] C. GEUZAINIE AND J.-F. REMACLE, *Gmsh: A 3-d finite element mesh generator with built-in pre- and post-processing facilities*, International Journal for Numerical Methods in Engineering, 79 (2009), pp. 1309 – 1331.
- [10] M. F. HAMILTON AND D. T. BLACKSTOCK, *Nonlinear acoustics*, vol. 237, Academic press San Diego, 1998.
- [11] B. KALTENBACHER, *Mathematics of nonlinear acoustics*, Evolution Equations and Control Theory, 4 (Sat Oct 31 20:00:00 EDT 2015), pp. 447–491.
- [12] B. KALTENBACHER AND I. LASIECKA, *Global existence and exponential decay rates for the Westervelt equation*, Discrete & Continuous Dynamical Systems-S, 2 (2009), p. 503.
- [13] B. KALTENBACHER, M. MELIANI, AND V. NIKOLIĆ, *Limiting behavior of quasilinear wave equations with fractional-type dissipation*, Advanced Nonlinear Studies, 24 (2024), pp. 748–774.
- [14] B. KALTENBACHER AND V. NIKOLIĆ, *Parabolic approximation of quasilinear wave equations with applications in nonlinear acoustics*, SIAM Journal on Mathematical Analysis, 54 (2022), pp. 1593–1622.
- [15] B. KALTENBACHER AND W. RUNDELL, *On an inverse problem of nonlinear imaging with fractional damping*, Mathematics of Computation, 91 (2022), pp. 245–276.
- [16] ———, *On the identification of the nonlinearity parameter in the Westervelt equation from boundary measurements*, Inverse Problems and Imaging, 15 (Thu Sep 30 20:00:00 EDT 2021), pp. 865–891.
- [17] B. KALTENBACHER AND A. SCHLINTL, *Fractional time stepping and adjoint based gradient computation in an inverse problem for a fractionally damped wave equation*, Journal of Computational Physics, 449 (2022).
- [18] A. KUBICA, K. RYSZEWSKA, AND M. YAMAMOTO, *Time-fractional differential equations: a theoretical introduction*, Springer, 2020.
- [19] V. P. KUZNETSOV, *Equations of nonlinear acoustics*, Soviet Physics: Acoustics, 16 (1970), pp. 467–470.
- [20] W. LAUTERBORN AND R. METTIN, *Nonlinear bubble dynamics: response curves and more*, Sonochemistry and sonoluminescence, (1999), pp. 63–72.
- [21] ———, *Acoustic cavitation: bubble dynamics in high-power ultrasonic fields*, in Power Ultrasonics, Elsevier, 2023, pp. 23–52.
- [22] J. H. LEE, W. Y. TEY, K. M. LEE, H.-S. KANG, AND K. Q. LEE, *Numerical simulation on ultrasonic cavitation due to superposition of acoustic waves*, Materials Science for Energy Technologies, 3 (2020), pp. 593–600.
- [23] M. J. Lighthill, *Viscosity effects in sound waves of finite amplitude*, Surveys in mechanics, 250351 (1956).
- [24] S. MEYER AND M. WILKE, *Optimal regularity and long-time behavior of solutions for the Westervelt equation*, Applied Mathematics & Optimization, 64 (2011), pp. 257–271.
- [25] K. MIZOHATA AND S. UKAI, *The global existence of small amplitude solutions to the nonlinear acoustic wave equation*, Journal of Mathematics of Kyoto University, 33 (1993), pp. 505–522.
- [26] K. E. MORGAN, J. S. ALLEN, P. A. DAYTON, J. E. CHOMAS, A. KLIBAOV, AND K. W. FERRARA, *Experimental and theoretical evaluation of microbubble behavior: Effect of transmitted phase and bubble size*, IEEE transactions on ultrasonics, ferroelectrics, and frequency control, 47 (2000), pp. 1494–1509.

- [27] B. E. NOLTINGK AND E. A. NEPPIRAS, *Cavitation produced by ultrasonics*, Proceedings of the Physical Society. Section B, 63 (1950), p. 674.
- [28] A. T. ORATIS, K. DIJS, G. LAJOINIE, M. VERSLUIS, AND J. H. SNOEIJER, *A unifying Rayleigh-Plesset-type equation for bubbles in viscoelastic media*, The Journal of the Acoustical Society of America, 155 (2024), pp. 1593–1605.
- [29] F. PRIEUR AND S. HOLM, *Nonlinear acoustic wave equations with fractional loss operators*, The Journal of the Acoustical Society of America, 130 (2011), pp. 1125–1132.
- [30] L. RAYLEIGH, *VIII. On the pressure developed in a liquid during the collapse of a spherical cavity*, The London, Edinburgh, and Dublin Philosophical Magazine and Journal of Science, 34 (1917), pp. 94–98.
- [31] G. SHAKYA, M. CATTANEO, G. GUERRIERO, A. PRASANNA, S. FIORINI, AND O. SUPPONEN, *Ultrasound-responsive microbubbles and nanodroplets: A pathway to targeted drug delivery*, Advanced Drug Delivery Reviews, 206 (2024).
- [32] M. VERSLUIS, E. STRIDE, G. LAJOINIE, B. DOLLET, AND T. SEGERS, *Ultrasound contrast agent modeling: a review*, Ultrasound in medicine & biology, 46 (2020), pp. 2117–2144.
- [33] R. VODÁK AND P. ŽENČÁK, *Mathematical analysis of an approximation model for a spherical cloud of cavitation bubbles*, Acta Applicandae Mathematicae, 154 (2018), pp. 43–57.
- [34] K. VOKURKA, *Comparison of Rayleigh's, Herring's, and Gilmore's models of gas bubbles*, Acta Acustica united with Acustica, 59 (1986), pp. 214–219.
- [35] B. WOLFRUM, *Cavitation and shock wave effects on biological systems*, PhD thesis, Citeseer, 2004.